

Full Length Article

Shedding light on the initial growth of ZnO during plasma-enhanced atomic layer deposition on vapor-deposited polymer thin films

Lisanne Demelius^a, Matthias Blatnik^b, Katrin Unger^a, Paola Parlanti^c, Mauro Gemmi^c, Anna Maria Coclite^{a,*}^a Institute of Solid State Physics, NAWI Graz, Graz University of Technology, Petersgasse 16, 8010 Graz, Austria^b CEITEC – Central European Institute of Technology, Brno University of Technology, Purkyňova 123, 612 00 Brno, Czech Republic^c Istituto Italiano di Tecnologia, Center for Materials Interfaces, Electron Crystallography, Viale Rinaldo Piaggio 34, 56025 Pontedera, Italy

ARTICLE INFO

Keywords:

Plasma
Polymer
Atomic layer deposition (ALD)
Initial growth
Etching
ZnO

ABSTRACT

Interest in atomic layer deposition (ALD) processes on polymer substrates is fueled by the increasing rise of organic electronics and polymer-based nanodevices. This study provides new insights into the initial growth and interface formation during plasma-enhanced ALD (PE-ALD) of ZnO on poly ethylene glycol dimethylacrylate (pEGDMA) and poly 2-hydroxyethyl methacrylate (pHEMA) thin films, both deposited by initiated chemical vapor deposition (iCVD). In-situ spectroscopic ellipsometry showed that PE-ALD growth on the investigated polymers is a result of two competing processes: plasma etching of the polymer substrate and ZnO nucleation and growth. During the first 10–15 ALD cycles, polymer etching was found to prevail until at a certain point (depending on plasma power and type of polymer) ZnO growth takes over and the regime of linear ALD growth is entered. On pHEMA, though more sensitive to etching, ZnO film formation starts early on, whereas on pEGDMA, subsurface nucleation and island growth appear to dominate the initial stage of deposition. Despite the initial etching, resulting ZnO films are smooth and of comparable structural quality to those grown on silicon. These findings contribute to a deeper understanding of PE-ALD growth on polymers providing knowledge essential for the successful development of new processes and applications.

1. Introduction

Atomic layer deposition (ALD) has gained an important place in the field of thin film deposition techniques in recent decades, as it can be used to deposit highly conformal films whose thickness can be precisely controlled. The advantages of ALD have led to its usage in a wide range of applications [1–12] that continues to expand as devices become smaller and feature increasingly complex 3D structures. The portfolio of materials that can be deposited via ALD encompasses many metals, insulators and semiconductors in both crystalline and amorphous phase [1,13].

In its early years, research on ALD was primarily directed towards the deposition on inorganic materials [14]. With the rise of organic electronics and other polymer-based systems, however, interest in thin film deposition on polymer substrates saw a steep increase. ALD has become an important method to deposit barrier and encapsulation layers for organic electronics [15] and photovoltaics [6,7], to functionalize polymeric materials for packaging [16] and biomedical

applications [17,18], as well as to fabricate anti-reflection coatings for plastics optics [19]. ZnO as a piezoelectric semiconductor material is particularly interesting for the application in flexible thin film transistors [20–22] and solar cells [23–28], transparent conductive oxides layers [29–31] and gas and strain sensors [32–34].

The use of thermal ALD proved ill-suited for depositing thin, conformal films on polymer substrates because precursor molecules can diffuse into the bulk of the polymer, leading to subsurface nucleation and growth [35,36]. This mechanism, though inconvenient for application cases which target sharp interfaces between the polymer layer and the thin film, is readily exploited in the field of vapor phase infiltration (VPI) where diffusion is maximized, e.g. by using longer precursor pulse times [37]. The extent of diffusion depends among others on the reactivity and miscibility between precursor and polymer, the size of the precursor molecule and the available free volume in the polymer [37,38]. A low reactivity of the precursor with the polymer generally results in more pronounced diffusion, while the presence of highly reactive groups (such as hydroxyl groups) limits reactions to the

* Corresponding author.

E-mail address: anna.coclite@tugraz.at (A.M. Coclite).<https://doi.org/10.1016/j.apsusc.2022.154619>

Received 27 May 2022; Received in revised form 11 August 2022; Accepted 18 August 2022

Available online 24 August 2022

0169-4332/© 2022 The Author(s). Published by Elsevier B.V. This is an open access article under the CC BY license (<http://creativecommons.org/licenses/by/4.0/>).

surface because adsorbing precursor molecules form a barrier layer for diffusion [37,39–41]. As an example, trimethylaluminum (TMA), the most commonly used precursor for Al_2O_3 deposition, undergoes reactions with hydroxyl, carbonyl and amine groups of the polymer but does not bind to methyl groups [36,37,42]. Diethylzinc (DEZ), a popular precursor for ZnO, strongly binds to hydroxyl groups [43], but in contrast to TMA, does not react as readily with carbonyl groups [44,45].

Nevertheless, in infiltration studies of ZnO (precursor exposure time > 5 min), the reaction between DEZ and carbonyl groups was reported [40,46].

A possible way to limit precursor diffusion and achieve a more ideal layer-by-layer growth with a sharp interface is to ensure a high density of reactive groups at the polymer surface that readily react with the precursor molecule. This can either be accomplished by plasma pre-treatments [47] or by using plasma-enhanced ALD (PE-ALD) instead of thermal ALD (or by choosing a polymer with an inherently high density of reactive groups). In PE-ALD, a plasma pulse replaces the otherwise gaseous co-reactant. Due to the high reactivity of the plasma, PE-ALD can achieve higher growth rates and operate at lower deposition temperatures [14,48], thus extending the spectrum of polymers that can be used as substrates. In addition, PE-ALD was observed to result in films with lower carbon impurity levels when compared to thermal ALD [49]. PE-ALD of inorganic thin films on polymer substrates has already been demonstrated for several applications cases [48–51], particularly for the deposition of barrier and encapsulation layers for organic electronics [52–56], but to date, little attention has been paid to the initial stages of growth and the formation of the interface between the polymer substrate and the PE-ALD thin film. A thorough understanding of the mechanisms determining nucleation and growth during PE-ALD on polymers is essential to enable the efficient design of high-quality devices.

It is well known that the exposure of polymer substrates to oxygen plasma results in the formation of hydroxyl and carboxyl groups at the surface [57–60], thus providing reactive sites for the ALD precursor. During PE-ALD, this inherent plasma surface activation was found to reduce nucleation delays [61] often observed for thermal ALD on polymers [62] and can be expected to decrease the infiltration depth of the precursor molecules into the polymer bulk [47]. Interface studies [55,63] of Al_2O_3 and TiO_2 deposited via PE-ALD on several polymer thin films with different functional groups found a varying degree of intermixing between the layers. Analogous to the trend observed for thermal ALD, polymers without any reactive groups experienced deeper precursor infiltration (>53 nm), while polymers rich in hydroxyl-groups showed significantly sharper interfaces.

In addition to surface activation, plasma is also prone to damage organic substrates by etching [58,64]. Napari et al. [61] showed that plasma damage is mainly caused by ion bombardment. To date, the potential impact of plasma etching during the early stages of PE-ALD on polymers has rarely been discussed or mentioned. Gebhard et al. [65] are the only ones so far who provided experimental evidence for simultaneous etch and growth processes by in-situ quartz crystal microbalance (QCM) measurements during PE-ALD of SiO_2 and Al_2O_3 on polypropylene (PP) films. Exactly how the interaction between plasma and polymer influences ALD growth and interface formation still lacks comprehensive study.

Our work aims to contribute to the understanding of PE-ALD processes on polymers by providing fundamental insights into PE-ALD growth of ZnO on different polymer thin films deposited via initiated chemical vapor deposition (iCVD). iCVD allows for the solventless deposition of polymers in the form of ultra-smooth and uniform films, and its combination with PE-ALD has rarely been investigated before. Growth of ZnO on the iCVD polymers was monitored via in-situ spectroscopic ellipsometry, and the resulting thin films were further characterized in terms of crystallinity, surface morphology and elemental composition. To gain a better understanding of how the chemical structure of the polymer influences precursor-substrate interactions and

with that the growth process, two different polymers were studied in detail, the first a methyl-terminated, crosslinked species containing carbonyl-groups (poly ethylene glycol dimethacrylate, pEGDMA), and the second a hydroxyl-terminated, linear polymer (poly 2-hydroxyethyl methacrylate, pHEMA). The dependence of growth on the plasma power applied during the PE-ALD cycles was examined for plasma powers between 30 and 100 W, and for a plasma power of 60 W, the first 25 cycles of PE-ALD growth were investigated in more detail. Our study shows that polymer chemistry and plasma power have a significant effect on the growth process. Based on these results, important factors influencing PE-ALD growth and interface formation on polymers could be identified and discussed.

2. Materials and methods

Polymer thin films of 2-hydroxyethyl methacrylate (HEMA, 97 %, Sigma-Aldrich, Vienna, Austria) and ethylene glycol-dimethacrylate (EGDMA, 98 %, Sigma-Aldrich, Vienna, Austria) were deposited on single side polished silicon (100) substrates with a native oxide layer (Siegert Wafer, Aachen, Germany) using a custom-built initiated chemical vapor deposition (iCVD) system described elsewhere [66]. The monomers HEMA and EGDMA were heated up to 75 and 85 °C, respectively, and were fed into the reactor at flow rates of 0.6 ± 0.1 sccm and 0.2 ± 0.1 sccm. The initiator *tert*-butyl peroxide (TBPO, 98 %, Sigma-Aldrich, Vienna, Austria) was kept at room temperature and its flow rate was maintained at 1.9 ± 0.2 sccm. During the deposition, the working pressure was kept at 200 and 500 mTorr for pHEMA and pEGDMA, respectively. The filament was heated up to 230 and 200 °C while the substrate was kept at 25 °C. Laser interferometry was used to monitor the film thickness and the depositions were stopped at an approximate thickness of 150 nm.

ZnO was deposited on top of the polymer thin films (and directly on silicon as a reference) by plasma-enhanced atomic layer deposition (PE-ALD) in a custom-built direct plasma reactor (detailed description can be found elsewhere [67]) at a substrate temperature of 35 °C. Diethylzinc (DEZ, Dockweiler Chemicals, Marburg, Germany) was used as the metalorganic precursor with oxygen plasma as co-reactant. Argon (20 sccm) was used as a carrier and purge gas. During plasma exposure, the oxygen pressure was kept at 200 ± 2 μbar and plasma powers were varied between 30 and 100 W. To ensure surface-limited growth, a growth kinetics study was performed for 60 W plasma power to determine the optimal pulse and purge times. The resulting saturation curves can be found in the [supplementary material \(Fig. A1\)](#) together with a detailed description of the pulse sequence of one PE-ALD cycle. In this study, ZnO films were grown with 100 cycles (resulting in a final thickness of approximately 20 nm) and 250 cycles (approximately 50 nm).

2.1. In-situ ellipsometry

To monitor the growth of the ZnO thin films, ellipsometry measurements (J.A. Woollam M-2000 V, Lincoln, NE, USA) were performed in-situ at an angle of incidence of 70.8° in a wavelength range from 370 to 1000 nm in dynamic acquisition mode (measurement every 3 s). Data analysis was performed with the software CompleteEASE® (J.A. Woollam, Lincoln, NE, USA). The silicon substrate and native oxide layer were modelled using tabulated optical functions with a fixed native oxide thickness of 1.22 nm. The homopolymer thin films were modelled by a Cauchy layer.

$$n(\lambda) = A + \frac{B}{\lambda^2} + \frac{C}{\lambda^4} \quad (1)$$

where n is the wavelength-dependent refractive index, λ is the wavelength and A , B and C are fit parameters. For pHEMA, thickness-dependent grading of the optical constants was included because it gave better fit results. The ZnO layer was modelled by a Cauchy layer

with an Urbach absorption term,

$$k(E) = k_0 e^{D(E-E_{\text{bandedge}})} \quad (2)$$

where k is the extinction coefficient, E the energy of the incoming light, k_0 and D are fitting parameters, and E_{bandedge} denotes the constant band edge energy. Due to high parameter correlation, D was fixed at a value of 1.5. Fitting was limited to the spectral range where ZnO is transparent, i.e. 450–1000 nm. The parameter C was set to 0 for both polymer and ZnO layer, as it did not significantly improve the fit results.

The fitting procedure of the dynamic in-situ data was as follows: Before the start of the deposition, the optical constants and the thickness of the polymer layer were fitted. Keeping the optical constants of the polymer layer fixed, the optical constants of the ZnO layer were fitted using a multi sample analysis (MSA) in order to minimize parameter correlation. For the MSA, a data set of 20 measurement points throughout the later part of the deposition, where polymer etching can be expected to have only negligible influence, was selected. The data was then fitted for a common polymer thickness and common optical constants of the ZnO layer, while the ZnO film thickness was allowed to differ for each measurement within the data set. Because parameter correlation between the two layer thicknesses (polymer and ZnO) was still high (>0.95 in the correlation matrix), the final thickness value of the ZnO layer (around 20 and 50 nm respectively) determined by X-ray reflectivity (XRR) (see section 2.2) was imposed on the MSA as an additional constraint.

In the last step, the optical constants for ZnO obtained by MSA were kept fixed and only the two thicknesses (polymer and ZnO) were allowed to vary during fitting of the full deposition process. As an additional constraint, the polymer film thickness was kept constant once several nanometers of ZnO were deposited on top. The error of the derived thickness values was determined by the interval within which the mean square error (MSE) of the fit increased by 50 %.

2.2. Ex-situ characterization methods

The vapor-deposited polymer thin films were characterized by Fourier-Transform Infrared (FT-IR) Spectroscopy (Bruker IFS 66v/S) to confirm the presence of functional groups. The transmission mode was used to record spectra in the range 500–4000 cm^{-1} with a resolution of 4 cm^{-1} at a chamber pressure of 8 mbar. During post-processing, all spectra were baseline corrected and normalized to their film thickness, i. e. the measured intensity was divided by the corresponding film thickness.

X-ray reflectivity (XRR, PANalytical Empyrean, Malvern Panalytical, Kassel, Germany) utilizing monochromatized copper radiation ($\lambda = 1.5418 \text{ \AA}$) was performed to gain information on film thickness, electron density and surface and interface roughness values. In the set-up, a 10-mm mask, a $1/32^\circ$ divergence slit and a P0.1 anti-scatter slit were used. The diffractometer's PIXcel^{3D}-detector was operated in receiving slit mode. Fitting of the measured data was performed with the software X'Pert Reflectivity (Panalytical, The Netherlands) applying a four-layer model consisting of a semi-infinite Si substrate, a native SiO_2 layer, a polymer and a ZnO layer. The ZnO and polymer density, the ZnO and polymer thickness and the surface and interface roughness values were chosen as fit parameters. Fixed values were used for the density of silicon $\rho_{\text{Si}} = 2.329 \text{ g/cm}^3$ and native oxide $\rho_{\text{Ox}} = 2.65 \text{ g/cm}^3$. Error estimation of the fitted parameters was performed with the in-built error analysis tool of the fit software.

To analyze the crystallinity of the 50-nm thick ZnO films, XRD measurements were performed on the same instrument in a $\theta/2\theta$ -configuration, using a $1/8^\circ$ divergence slit and a P7.5 anti-scatter slit and operating the detector in its 1D-mode. For the thinner 20-nm ZnO films, a $\omega/2\theta$ -configuration with a constant incident angle $\omega = 0.3^\circ$ was chosen to increase the sensitivity of the measurements. For this configuration, the $1/8^\circ$ divergence slit was exchanged by one with $1/32^\circ$.

Estimations for the average crystallite size D were obtained using Scherrer's formula [68],

$$D = \frac{\lambda}{\beta_{2\theta} \cos \theta} \quad (3)$$

where λ is the wavelength of the X-rays, $\beta_{2\theta}$ the full width at half maximum (FWHM) of the diffraction peak and θ is the peak position.

A Nanosurf Easyscan 2 (Nanosurf, Liestal, Switzerland) equipped with a C3000 controller was used to obtain atomic force microscopy (AFM) images. Measurements were performed in tapping mode with a Tap190Al-G cantilever (BudgetSensors, Bulgaria). Image post-processing and data analysis were carried out with the free software package Gwyddion [69]. Error estimation was performed by averaging over backward- and forward scan and over images acquired at different spots on the sample surface.

A dual beam FIB-SEM Helios Nano Lab 600i (Thermo Fisher Scientific, Waltham, MA, USA) was used for characterizing the ZnO/pEGDMA and ZnO/pHEMA interfaces. Cross-sections were obtained using a gallium beam operating at 30 kV and 790 pA perpendicular to the surface. SEM images of the cross-sections were acquired at a sample tilt of 52° and a working distance of 4 mm with a Through-the-Lens-Detector (TLD) at 2 kV and 43 pA landing current using secondary electrons (SE) detection.

X-ray fluorescence (XRF) spectroscopy was performed with a PANalytical Epsilon 1 (Malvern Panalytical, Kassel, Germany) to determine the relative Zn content after different deposition cycles. The Ag anode X-ray tube was operated at a voltage of 50 kV and a current of 100 μA . Measurements were carried out with a 100- μm Ag filter and the Zn-K α peak height at 8.63 keV was evaluated by Gauss-fitting.

X-ray photoelectron spectroscopy (XPS) was performed with a Kratos Axis Supra+ (Kratos Analytical, Manchester, UK) using monochromatic Al K α radiation with an energy of 1486.6 eV. Measurements were conducted in fixed analyzer transmission mode and at different emission angles (0 and 70°). A pass energy of 160 eV and 20 eV and a step size of 1 eV and 0.1 eV were used for survey and high-resolution scans, respectively. The samples were measured without any further surface treatment and charge compensation was achieved via the in-built charge neutralizer system. Data analysis and component fitting was performed with the software CasaXPS (Casa Software Ltd., Teignmouth, UK). All spectra were calibrated with respect to the C-C adventitious carbon peak at 284.8 eV.

3. Results and discussion

Prior to ZnO deposition, the polymer thin films used as substrates were characterized in terms of chemical composition, thickness and roughness. The results show that both pEGDMA and pHEMA thin films are between 140 and 210 nm thick, highly uniform and smooth (see AFM images in Fig. 1a). The roughness values determined from XRR measurements are $1.0 \pm 0.2 \text{ nm}$ and $0.7 \pm 0.2 \text{ nm}$ for pEGDMA and pHEMA, respectively. Fourier-transform infrared (FT-IR) spectra of the polymer thin films (Fig. 1b) clearly show the presence of the expected functional groups (the chemical structures of the polymers are displayed in Fig. 1c-d). Both polymers exhibit an absorption band corresponding to C=O and C—O stretching at 1730 cm^{-1} and between 1000 and 1300 cm^{-1} , respectively. pHEMA shows an additional broad absorption band around 3000 cm^{-1} corresponding to O—H stretching.

3.1. PE-ALD on iCVD polymers at different plasma powers

ZnO was deposited via PE-ALD on thin polymer films of pEGDMA and pHEMA using plasma powers between 30 and 100 W. The substrates were exposed to 100 ALD cycles resulting in a final ZnO film thickness of approximately 20 nm. In-situ spectroscopic ellipsometry was employed to monitor the thickness evolution of the two individual layers, polymer and ZnO.

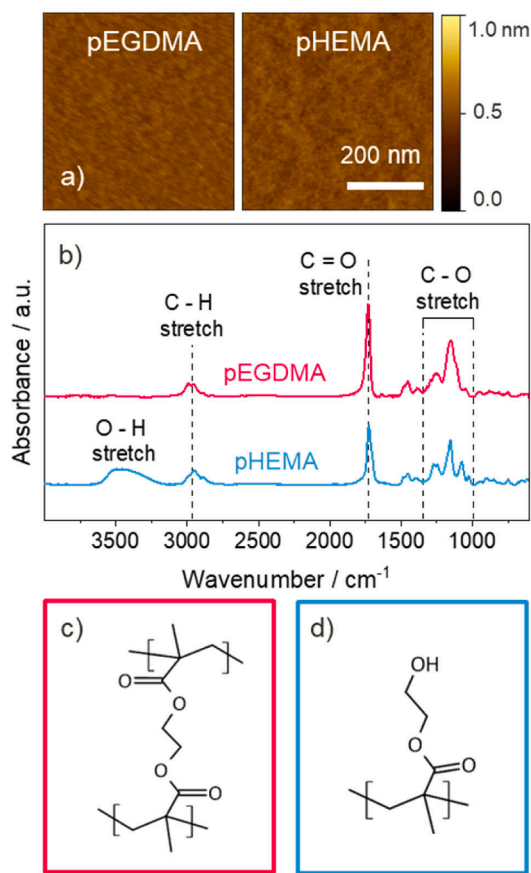


Fig. 1. Characterization of pEGDMA and pHEMA thin films deposited by iCVD: (a) AFM micrographs, (b) FT-IR spectra recorded in transmission mode with indication of the characteristic absorption bands, (c-d) chemical structure of pEGDMA (c) and pHEMA (d).

Fig. 2 shows the change of the polymer thickness Δt_{poly} with respect to the initial thickness, the ZnO thickness t_{ZnO} and the change of the total thickness $\Delta t_{\text{total}} = \Delta(t_{\text{poly}} + t_{\text{ZnO}})$ during the first 50 PE-ALD cycles for deposition on pEGDMA and pHEMA, respectively, as obtained from fitting the ellipsometry data using the approach described in section 2.1. Any major shifts in film thicknesses caused by correlations between the fit parameters are corrected by including the final thickness values determined by XRR into the fit process. The small step-like fringes that can be observed in the thickness evolution originate from the alternating precursor and plasma pulses. In an ideal ALD cycle, the precursor adsorption results in a thickness increase while plasma exposure leads to a decrease in thickness as oxygen reacts with the precursor leading to the removal of its organic ligands [70,71]. The results show that during PE-ALD, the film thicknesses follow the same general shape for both types of polymer substrates and all investigated plasma powers between 30 and 100 W. Three regimes can be identified in the curves: During the first stage of the PE-ALD process (regime I), instead of growth, an overall decrease in total thickness (Fig. 2a-b) can be observed. This thickness loss is due to plasma etching of the polymer (Fig. 2e-f). In regime I, no or very little ZnO growth is detected (Fig. 2c-d). At a specific point, the total thickness approaches a minimum, after which it gradually starts to rise again, eventually settling on a linear increase. The minimum in total thickness (indicated by the vertical dotted lines in Fig. 2a-b) is due to a shift from polymer etching to ZnO growth as the dominating mechanism. This transition can be attributed to incipient ZnO nucleation, which gradually inhibits polymer etching until a closed ZnO film is formed that blocks any further etching. Once polymer etching has subsided completely, the ZnO growth reaches a steady state with a constant

growth per cycle (GPC). The region from the on-set of ZnO growth until the steady state is reached is denoted as regime II, while the region of ideal linear ALD growth is referred to as regime III.

Even though these three regimes can be identified in all data sets in Fig. 2, the detailed thickness evolution depends on the type of polymer substrate and the plasma power, the latter having a strong influence on the strength and extent of polymer etching.

At 30 W, polymer etching is comparatively weak and overruled by ZnO film growth within only a few cycles. For pEGDMA, the transition from etching to growth occurs after 3 ALD cycles (Fig. 2a) with a total polymer thickness loss of 0.8 ± 0.4 nm (Fig. 2e). For pHEMA, the transition occurs after 5 cycles (Fig. 2b) with a slightly higher total polymer thickness loss of 1.3 ± 0.3 nm. Though the transition between etching and growth is rather abrupt, the initial GPC is lower and only reaches the steady state (regime III) after approximately 15 cycles. This behavior (delayed growth with a GPC that gradually approaches the steady-state value) is typical for substrate-inhibited growth type I (as defined by Puurunen et al. [72]). It should be noted that at 30 W, the observed polymer thickness decrease is on the order of the surface roughness (see above). As the used ellipsometry model does not account for surface roughness, it cannot be excluded that the thickness change arising from the fit is caused by a change in roughness.

Increasing the plasma power greatly enhances the impact of polymer etching. For pEGDMA, an overall decreasing trend in total thickness can be observed for as long as 16, 21 and 22 cycles for plasma powers of 60, 80 and 100 W, respectively (Fig. 2a), and total polymer thickness losses are 23 ± 1 nm, 43 ± 1 nm and 62 ± 1 nm (Fig. 2c). For pHEMA, the minimum in total thickness is reached after 21–22 cycles and total polymer thickness losses of 35 ± 1 nm, 59 ± 1 nm and 83 ± 1 nm (corresponding to plasma powers of 60, 80 and 100 W) are 35–50 % higher than for the first polymer. As can be seen in Fig. 2c-d, the stronger etching leads to a delay in ZnO film formation. On pEGDMA, no ZnO nucleation is detectable during the first 12–17 cycles followed by a steep on-set of growth with a GPC value higher than that of the steady state. The steady state (regime III) is reached after approx. 25–30 cycles. On pHEMA, ZnO nucleation appears to start already during the first ALD cycles, despite the stronger etching of the polymer substrate, and the on-set of growth is shallower compared to pEGDMA. The steady state is reached after approx. 30 cycles.

The thickness evolution of ZnO deposited on pEGDMA at plasma powers between 60 and 100 W is typical for substrate-inhibited growth type II. This growth mode, as defined by Puurunen et al. [72], is characterized by an initially low GPC that undergoes a maximum until it decreases to the steady state, and has repeatedly been associated with island growth [72–74]. The maximum of the GPC is due to the growing islands that provide a larger surface area available for deposition, resulting in an enhanced deposition rate. Once the islands start to coalesce, the GPC gradually decreases to its steady-state value. Island growth of ZnO has been previously observed on silicon substrates with a native oxide layer [75,76]. Compared to pEGDMA, the gradual growth on-set of ZnO on pHEMA resembles more a layer-by-layer growth, though some island contribution with a temporarily enhanced GPC is still visible. A possible reason for the more pronounced island growth on pEGDMA could be a lower density of reactive surface groups that serve as nucleation sites. A lower density of nucleation sites results in a lower density of islands, which in turn grow larger until they coalesce into a continuous film. Since the polymer's carbonyl groups are known to react only weakly with DEZ, nucleation sites can be assumed to originate mainly from plasma activation. On pHEMA, the inherent hydroxyl groups can be expected to increase the density of nucleation sites, thus leading to more and smaller islands that coalesce into a closed layer more quickly.

The presence of island growth during the initial phase of film formation could also explain the simultaneous occurrence of ZnO growth and etching during the transition regime (II), since part of the polymer substrate remains exposed to the oxygen plasma until the islands

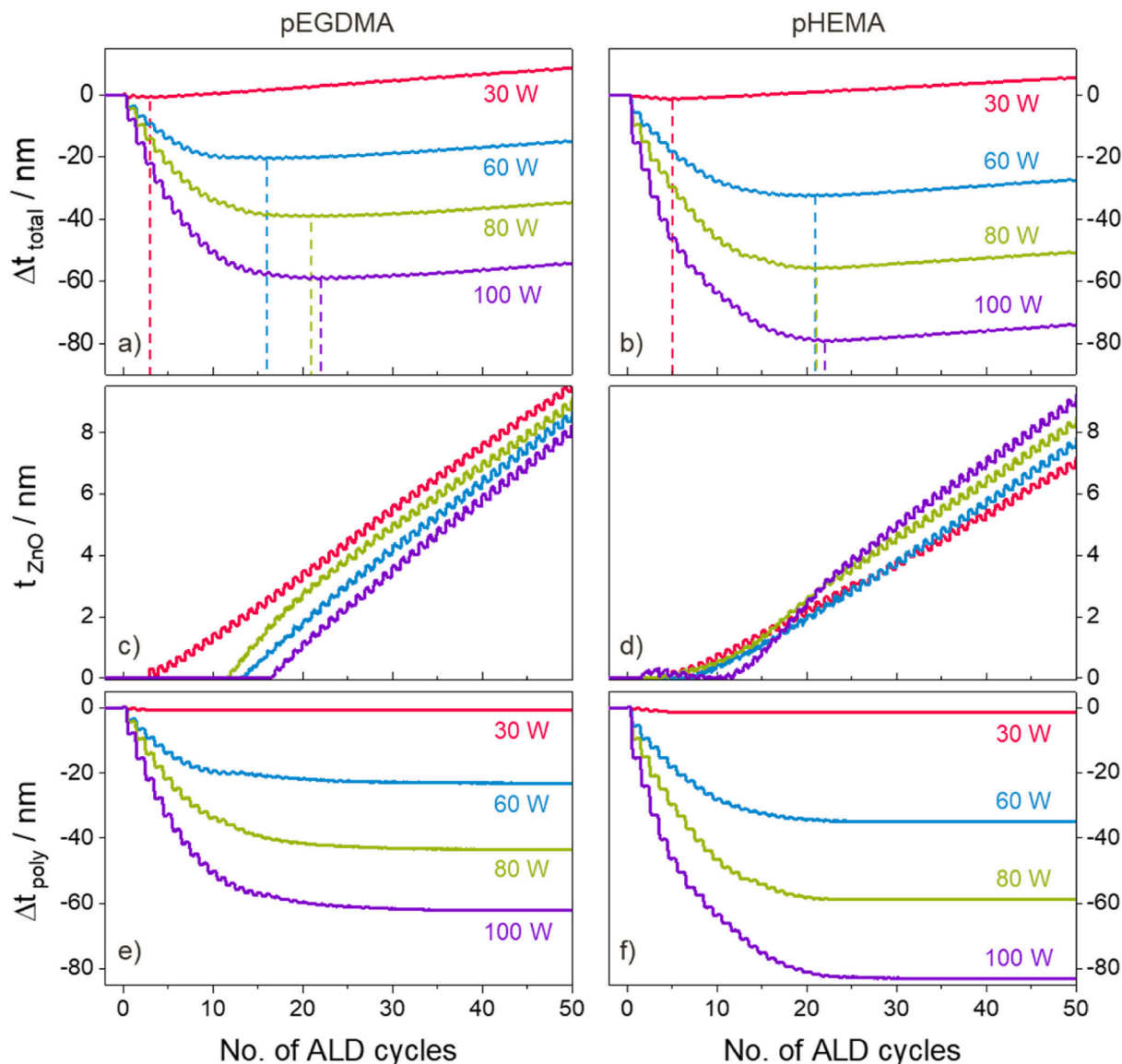


Fig. 2. Fitted in-situ ellipsometry results showing the layer thickness evolution during the first 50 cycles of ZnO PE-ALD on pEGDMA and pHEMA for different plasma powers: (a-b) change in total thickness Δt_{total} (polymer + ZnO), (c-d) ZnO thickness t_{ZnO} , and (e-f) change in polymer thickness Δt_{poly} for deposition on pEGDMA (a,c,e) and pHEMA (b,d,f), respectively. Dashed vertical lines in (a-b) indicate the position of the minima. The thickness changes Δt_{poly} and Δt_{total} are given with respect to the initial thicknesses before the deposition.

coalesce. It should be noted here that in order to confirm the hypothesis on island growth discussed above, additional experimental evidence such as SEM surface analyses is required which will be the subject of a future study.

For plasma powers between 60 and 100 W, the GPC values in the linear regime (III) of the deposition are around $2.1 \pm 0.1 \text{ \AA/cycle}$ for both polymers, in agreement with the reference values measured for growth of ZnO directly on silicon at 60 W ($2.1 \pm 0.1 \text{ \AA/cycle}$, see Fig. A2). This indicates that after a certain initial phase, the ZnO forming on the surface is no longer influenced by the type of substrate. An exception is ZnO growth on the polymer at 30 W plasma power, where the observed GPC values are lower. This is likely due to incomplete surface reactions. Since the used ALD recipe was optimized for a plasma power of 60 W and the thus determined process parameters might not be ideal at lower plasma powers. It must be noted that while the growth process in regime III can be expected to be sufficiently well described by the used ellipsometry model (a stack of flat, uniform layers), the model approaches its limits when fitting the initial stage of ZnO, since it does not account for surface roughness or island growth.

Although the uniqueness of fit is generally good, parameter correlations between the polymer thickness and the ZnO thickness are high (correlation matrix elements with values > 0.97). Moreover, the fit model assumes that the dielectric functions of the layers remain constant throughout the entire deposition. It can be expected, however, that the first few layers of ZnO have optical constants that differ from the ones used in the ellipsometry model, e.g. due to intermixing of the polymer and ZnO. For these reasons, film thicknesses determined during the early stages of growth should only be viewed as ‘apparent’ thickness values that might differ from the real physical quantity.

Although the ellipsometry-derived thickness values for the initial stage of growth might not directly correspond to the actual layer thicknesses, differences in growth onset and the extent of plasma etching are nonetheless clearly visible between the two polymer substrates. This indicates that the type of substrate does have an impact on the nucleation and film formation of ZnO.

3.2. Initial growth at 60 W

In order to validate the in-situ ellipsometry results and get a deeper understanding of the mechanisms driving the transition from polymer etching to ZnO growth at the initial stages of growth, additional ex-situ XRR and XRF measurements were performed at 5-cycle intervals during the first 25 cycles of PE-ALD on both pEGDMA and pHEMA at 60 W plasma power. The plasma power of 60 W was selected because differences between the ZnO growth behavior were clearly visible at this power while, at the same time, the etching loss was kept to a medium level.

Fig. 3a shows that ZnO film thicknesses derived from XRR exhibit the same trend as the in-situ ellipsometry results. On pHEMA, the presence of a top layer is already clearly visible after 5 ALD cycles while no film formation can be detected on pEGDMA until cycle no. 15. Similar to the ellipsometry results, ZnO growth on pHEMA exhibits a gradual on-set while the on-set of growth is steeper on pEGDMA. Plots of the individual XRR measurements and their fits can be found in the [supplementary material](#) (Fig. A3). Despite the apparent differences in growth delay and on-set, XRF results (Fig. 3b), displaying the height of the zinc $K\alpha_2$ -peak as a measure for the zinc content in the sample, show that zinc can be detected in both polymer samples from the very start. For both polymers, the zinc content increases in a roughly linear fashion without any visible delay. Contrary to what one would expect based on the ellipsometry and XRR results, zinc contents measured on pEGDMA are slightly higher than those measured on pHEMA. A possible explanation for the higher amount of zinc on pEGDMA and its detection prior to film formation could be that part of the zinc detected by XRF is located below the surface, e.g. due to precursor diffusion into the polymer.

As mentioned in the introduction, sub-surface diffusion of precursors is a well-known phenomenon for thermal ALD on polymer substrates [35,36]. Even though the use of plasma as a co-reactant was shown to greatly enhance surface growth by generation of reactive groups on the polymer surface, several research groups still observed some degree of

interdiffusion. Perrotta et al. [55] performed XPS depth-profiling on Al_2O_3 thin films deposited on Poly(3-hexylthiophen-2,5-diyl):indene-C60 bisadduct (P3HT:ICBA) and found infiltration depths of Al_2O_3 into the polymer of 6–9 nm at 30 °C deposition temperature and up to 15 nm at 80 °C. Bulusu et al. [63] observed intermixing at the interfaces for Al_2O_3 and TiO_2 deposited on a hydroxyl-group- and an amine-group-rich polymer by time-of-flight secondary ion mass spectroscopy (ToF-SIMS). Although the infiltration depths were not quantified, a qualitative comparison showed that diffusion was more pronounced for the amine-rich polymer, which can be expected to be less reactive with the precursor. For PE-ALD of Al_2O_3 on polyethylene naphthalate (PEN), Kim et al. [54] observed rough interface layers of approximately 10 nm thickness by high resolution TEM imaging, which were attributed to interdiffusion. However, the initial roughness of the PEN substrate was not mentioned. It must be noted that in all three studies a remote plasma source was used where little to no etching can be expected, though only the first study experimentally confirmed the absence of polymer etching.

Based on these previously published results, it seems reasonable that sub-surface diffusion plays a role for the polymers studied in this work as well. The more pronounced infiltration in the case of pEGDMA, as suggested by the XRF results, is likely due to pEGDMA's less reactive carbonyl-groups as compared to the highly reactive hydroxyl groups in pHEMA.

To gain further insight into the surface composition at the early stages of growth, XPS was measured on samples that were exposed to 5 cycles of PE-ALD, i.e. at a stage where according to XRR and in-situ spectroscopic ellipsometry (SE) film formation has already started on pHEMA but not on pEGDMA (Fig. 3a).

The pronounced Zn 2p peak doublets in the survey scans in Fig. 4a clearly show that zinc is present on both samples (pEGDMA and pHEMA), which is in agreement with the XRF results. The scan also reveals significant amounts of oxygen and carbon, as can be seen from the heights of the O 1s and C 1s peaks. This is hardly surprising, since first, the sample surface was not cleaned prior to XPS analysis to remove

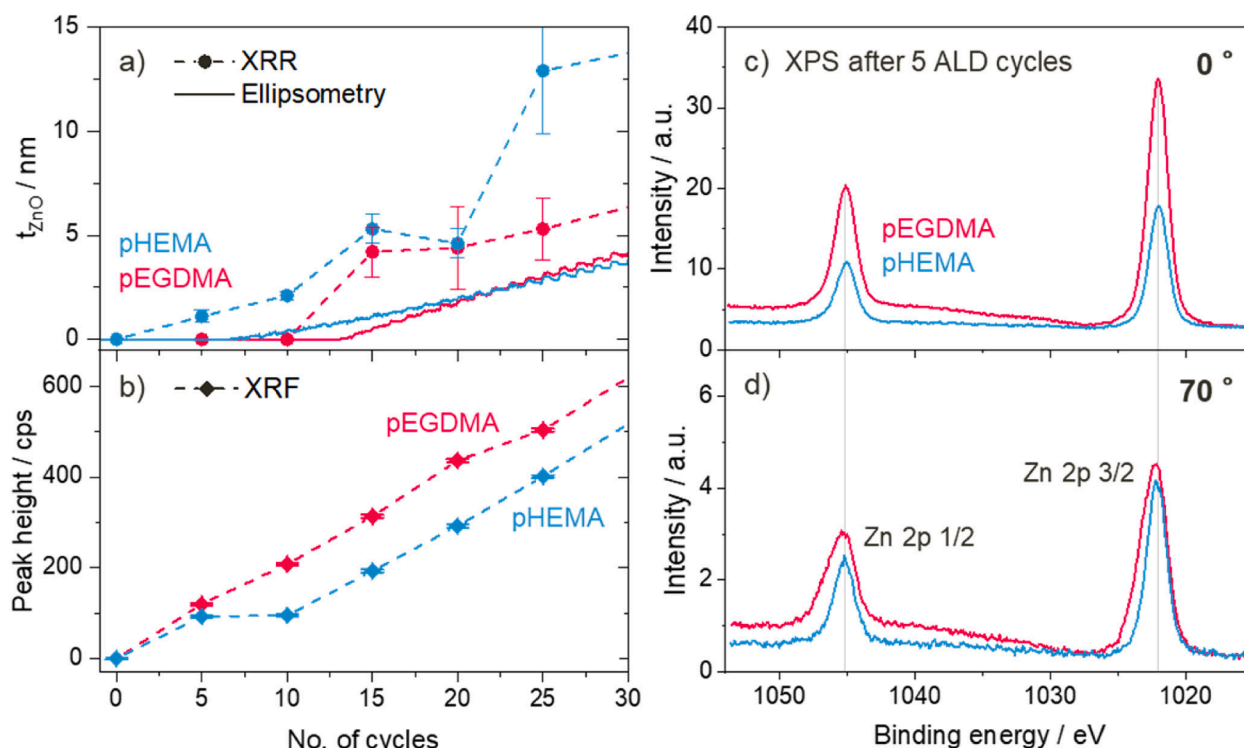


Fig. 3. Comparison of the initial growth of ZnO at 60 W plasma power on pEGDMA and pHEMA. (a) Comparison of fitted in-situ ellipsometry results to thickness values derived from fitting ex-situ XRR measurements, (b) XRF peak height of the $K\alpha_2$ -peak of zinc during the initial 25 cycles of deposition, and (c-d) XPS high resolution spectra of pEGDMA and pHEMA after 5 ZnO PE-ALD cycles showing the Zn 2p doublet peak at different emission angles: (c) 0° and (d) 70°.

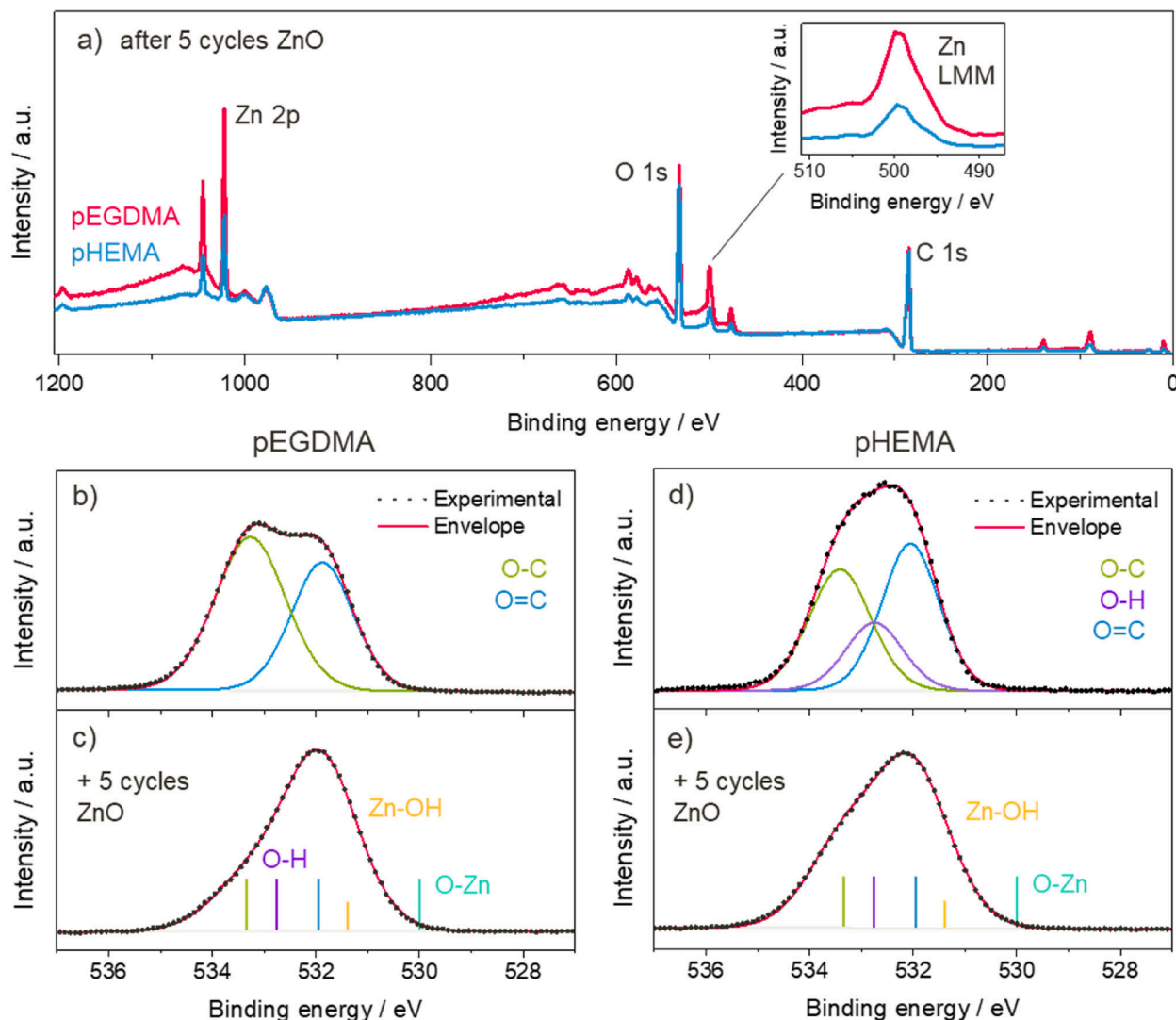


Fig. 4. XPS spectra. (a) XPS survey scans (raw data) of pEGDMA and pHEMA thin films after exposure to 5 ZnO PE-ALD cycles. Inset shows a magnified view of the Zn $L_{2,3}M_{4,5}M_{4,5}$ Auger peak. (b–e) High resolution XPS spectra of the O 1s peak for (b,c) pEGDMA and (d,e) pHEMA before (b,d) and after (c,e) exposure to 5 ZnO PE-ALD cycles. Dotted lines show the raw experimental data. Solid lines correspond to fitted peaks. The background is displayed in light grey. In (c) and (e), expected positions of the component peaks are indicated by vertical lines.

any surface contamination layers, and second, significant signal contribution from the polymer substrate is to be expected since 5 ALD cycles correspond to only about 1 nm nominal ZnO film thickness at a GPC of 2.1 Å/cycle. High-resolution scans of the Zn 2p doublet peaks are displayed in Fig. 3c. The Zn 2p 3/2 and 1/2 peak are located at around 1022.1 ± 0.1 eV and 1045.2 ± 0.1 eV, respectively, with a difference in binding energy (BE) of 23.1 eV which corresponds well to values reported in literature [77–80]. From the Zn 2p peak positions alone one cannot reliably determine the oxidation state, but the position of the Zn $L_{3}M_{4,5}M_{4,5}$ Auger transition (see inset in Fig. 4a) at a binding energy of 507.9 ± 0.1 eV can be unambiguously assigned to a Zn^{2+} oxidation state [81–83]. The modified Auger parameter was calculated for the Zn $L_{3}M_{4,5}M_{4,5}$ Auger peak and the Zn 2p 3/2 core level peak using the following formula.

$$\alpha' = E_{kinetic}(ZnL_{3}M_{4,5}M_{4,5}) + BE(Zn2p_{3/2}) \quad (4)$$

And gives further insight into the binding state of zinc. For both polymer substrates, the modified Auger parameter α' is 2009.5 ± 0.1 eV, a value that is characteristic for $Zn(OH)_2$ (stoichiometric ZnO typically has a modified Auger parameter of 2010.2 ± 0.4 eV, and metallic Zn has an even higher value of 2013.8 ± 0.3 eV) [81]. This suggests that the

zinc present in the samples is mainly bonded to hydroxyl groups, and also possibly to oxygen-carbon species from the polymer structure, forming hybrid bonds. Due to the linear nature of the DEZ precursor molecule, ZnO can grow by maximum one Zn-O entity per cycle (since only one bond is available), evolving from a mono ($-Zn-OH$) to a dimer ($-Zn-O-Zn-OH$) to a trimer zinc configuration, and so on. Ocola et al. [84] performed a detailed study of the first few cycles of ZnO vapor phase infiltration in poly methyl methacrylate (PMMA) and showed that under saturation conditions, the first signs of stoichiometric ZnO with wurtzite crystal structure can be observed after 3 cycles at the earliest. Based on these results, it is reasonable that 5 cycles of PE-ALD on a polymer (where saturation conditions are unlikely to be met) do not yet result in stoichiometric ZnO.

In terms of height of the high-resolution Zn 2p peaks in Fig. 3c, a clear difference is observable between the two polymer substrates with a peak intensity on pEGDMA that is approximately twice as high as on pHEMA. Because the signal intensity of photoelectrons excited at atoms at higher depths is attenuated exponentially with the distance the electrons travelled through the sample, the peak height not only depends on the quantity of material but also on its in-depth distribution [85]. Additional angle-resolved (AR-XPS) measurements that provide a

higher surface sensitivity were performed at an emission angle of 70° in order to obtain further information. The resulting spectra in Fig. 3d show almost equal peak intensities on both polymers but a significant difference in their full width half maxima (FWHMs) that was not observed at normal emission. While Zn 2p peaks on pHEMA have FWHM values of approximately 1.8 eV, roughly 2.4 eV are observed on pEGDMA. The observation that Zn 2p peak heights are roughly the same for both polymers at 70° emission angle, indicates that similar amounts of zinc can be found in the topmost surface layers. As far as in-depth sensitivity of XPS allows, the higher zinc signal intensity for pEGDMA at normal emission (Fig. 3c) implies that overall, significantly more zinc can be found in pEGDMA samples. One possible interpretation is that the zinc species in pEGDMA extend deeper into the polymer. This hypothesis is further supported by analyzing the differences in background between the two polymers. Tougaard [85–87] demonstrated via theoretical and experimental analyses that the shape of the background in XPS spectra can provide important information on the in-depth distribution of the studied material. The further photoelectrons have to travel through the sample the more energy they lose due to inelastic scattering. These lower energy photoelectrons show up as an increased background on the higher BE side of the characteristic XPS peaks. In Fig. 3c–d (as well as Fig. 4a), the increase in background on the higher BE side of the Zn 2p peaks is significantly larger for ZnO on pEGDMA, suggesting that part of the zinc signal originates from greater depths. This is in agreement with the hypothesis formed based on the ellipsometry, XRR and XRF results, which also suggested that sub-surface diffusion is more pronounced in pEGDMA. The larger FWHM of the Zn 2p peaks at 70° emission may indicate that the zinc atoms near the surface of pEGDMA are in a more diverse binding environment with a broader range of binding energies as compared to pHEMA.

Fig. 4b–e displays the high-resolution O 1s peaks for pEGDMA and pHEMA before and after exposure to 5 ZnO ALD cycles (The high-resolution C 1s peaks can be found in the [supplementary material](#), Fig. A4). The peak for pristine pEGDMA (Fig. 4b) can be deconvoluted into two component peaks at roughly 533.4 and 532.0 eV, corresponding to O—C and O=C bonds, respectively [88–90]. For pristine pHEMA, an additional peak at 532.8 eV was introduced to account for the hydroxyl groups (O—H bonds) of pHEMA. These results agree well with the FT-IR spectra in Fig. 1b and reflect the chemical structure of the respective polymer. Slight deviations in the peak area ratios can be attributed to the additional presence of surface contaminations from the ambient, e.g., water, hydrocarbons, etc., that contain similar oxygen bonds. After exposure to 5 ZnO ALD cycles, the O 1s peaks for both polymers (Fig. 4c and e) change shape and shift towards lower binding energies. If stoichiometric ZnO was present in the samples, this would show up as an O-Zn peak component at a binding energy between 529.8 and 530.6 eV [77,78,91–96]. The data clearly shows that no such peak is present (the expected position of the O-Zn peak is indicated in Fig. 4c and e). This is consistent with the modified Auger parameter calculated above, which showed that the zinc in the samples is present in a hydroxylated state and not as stoichiometric ZnO. In literature, zinc hydroxide, non-stoichiometric ZnO and defect-like Zn—O—H bonds are often associated with a component peak at around 531.5 eV, as indicated in Fig. 4c and e [77,93,95,96]. The presence of such a peak could account for the shift of the envelope towards lower binding energies (see Fig. 4c and e). Apart from a component peak corresponding to the hydroxylated zinc, a significant contribution from the peaks associated with the polymer (O—C, O—H and O=C) can be expected. However, due to the polymer etching and surface modification (e.g. generation of hydroxyl and carboxyl groups) during the plasma steps, strong changes of the respective peak areas are likely to occur. Since the exact ratios between the different component peaks are of little interest for the main conclusions drawn from the data, the expected peak positions have been indicated by vertical lines only. It should be noted that the presented XPS measurements were only performed on one sample per polymer and condition (before and after exposure to 5 ALD cycles) in a representative

manner. However, measurements obtained at different locations on the same sample gave highly consistent results, indicating a very homogeneous surface.

Based on the results presented so far, several mechanisms can be identified that influence the initial growth process of ZnO on the two polymers, pEGDMA and pHEMA. As Fig. 2 showed, the plasma-induced polymer etching leads to a growth delay. At the same time, it is known that oxygen plasma activates the surface and thus accelerates nucleation. This enhancement of nucleation can be seen in Fig. 2 for 30 W plasma power. On both polymers, ZnO growth starts with a minimal delay of 3–5 cycles, whereas in the case of thermal ALD, where no plasma is used, a significant nucleation delay would be expected on pEGDMA with its weakly reactive carbonyl groups, while nucleation should be faster on the hydroxyl-rich pHEMA. At higher plasma powers, the effect of plasma etching is stronger and differences between the nucleation behavior on the two polymers are more evident. XRR and in-situ ellipsometry results (Fig. 2 and 3a) showed that film formation starts early on in the case of pHEMA while it is more delayed on pEGDMA. This is in contrast with the strength of polymer etching, which is 35–50 % higher for pHEMA, and indicates that the etching strength is not the only factor determining the growth delay. Instead, the results indicate that despite the plasma-induced generation of reactive surface groups that promotes growth on both polymers, the initial polymer chemistry still has a direct impact on nucleation, too. The steep on-set of ZnO growth on pEGDMA in Fig. 2 and 3a with a temporarily enhanced GPC was associated with island growth, and XRF and XPS results suggested a certain extent of sub-surface diffusion and growth on pEGDMA, both behaviors that would be expected for a polymer that has no or only weakly reactive functional groups. pHEMA with its highly reactive hydroxyl groups, on the other hand, exhibited a more surface-limited layer-by-layer like growth. This suggests that although the plasma generates additional nucleation sites, the inherent density of reactive sites still has an impact on the nucleation behavior.

The schematic in Fig. 5 is based on the above considerations and hypotheses and illustrates the differences between the initial growth on the two polymers. In the case of pHEMA, stronger etching is observed together with the early formation of a surface-limited ZnO layer presumably due to a higher density of nucleation sites. On pEGDMA, etching is found to be weaker and a lack of reactive polymer groups leads to more pronounced sub-surface diffusion and thus a more diffuse layer. Because the hypothesis on island formation lacks complementary experimental evidence, such as SEM surface analyses, it is not included in the schematic. The confirmation of island growth should be the subject of a subsequent study.

3.3. Effect of etching on ZnO thin film properties

To evaluate whether and how the plasma etching influences the quality of the grown ZnO thin films, thicker films (20 and 50 nm) grown at different plasma powers were analyzed with respect to their surface and interface roughness, ZnO density and crystallinity, and compared to films deposited directly on a silicon wafer where no substrate etching occurs. Cross-sectional SEM images of 50-nm thick ZnO films on pEGDMA and pHEMA (Fig. 6a–b) show a sharp transition between ZnO and the polymer, indicating that the intermixing at the interfaces discussed in the previous section must be limited to the region close to the interface and does not play a role on the thickness scale of the entire film. The interface between polymer and ZnO shows the presence of 3D nanoflakes that cause a certain degree of roughening, which is more pronounced in the case of pEGDMA. This could be due to the island formation dominating the initial phase of ZnO growth. Another indication that intermixing only occurs close to the interface is given by the XRR measurements of 20-nm thick ZnO films on polymer (see Fig. A5) which clearly show the superposition of Kiessig fringes corresponding to two distinct layer thicknesses.

AFM measurements of 20-nm thick ZnO films show that the surface

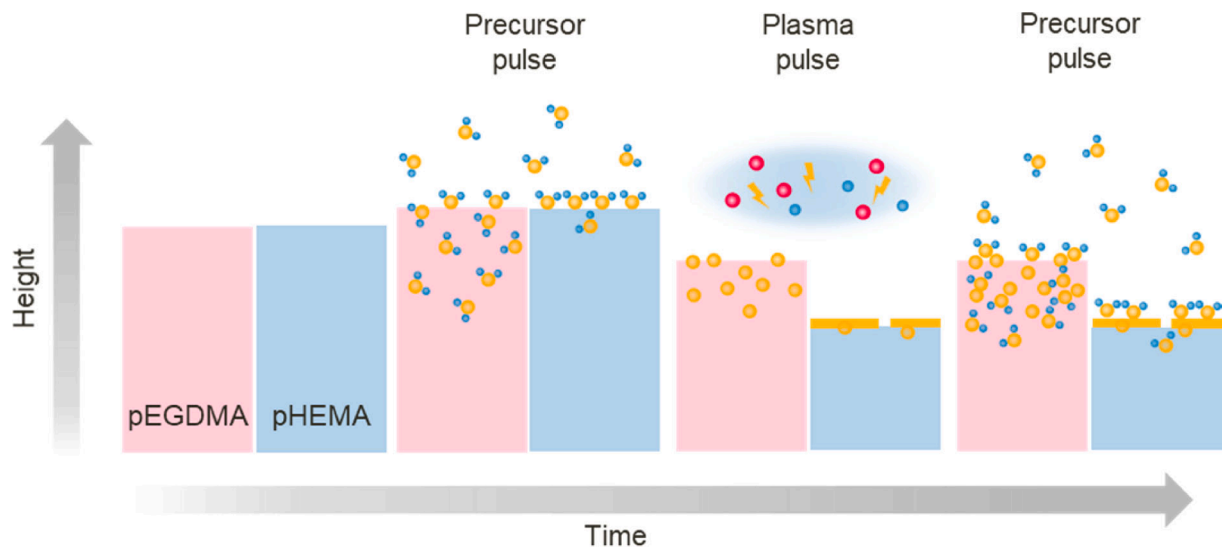


Fig. 5. Schematic of the differences between initial ZnO nucleation on pEGDMA and pHEMA at 60 W plasma power. Zinc atoms are depicted as yellow spheres, ethyl groups are shown in blue. The red spheres represent oxygen atoms. For simplicity, reacted ZnO is shown in yellow as well, omitting the oxygen component in the depiction of ZnO nuclei and thin films.

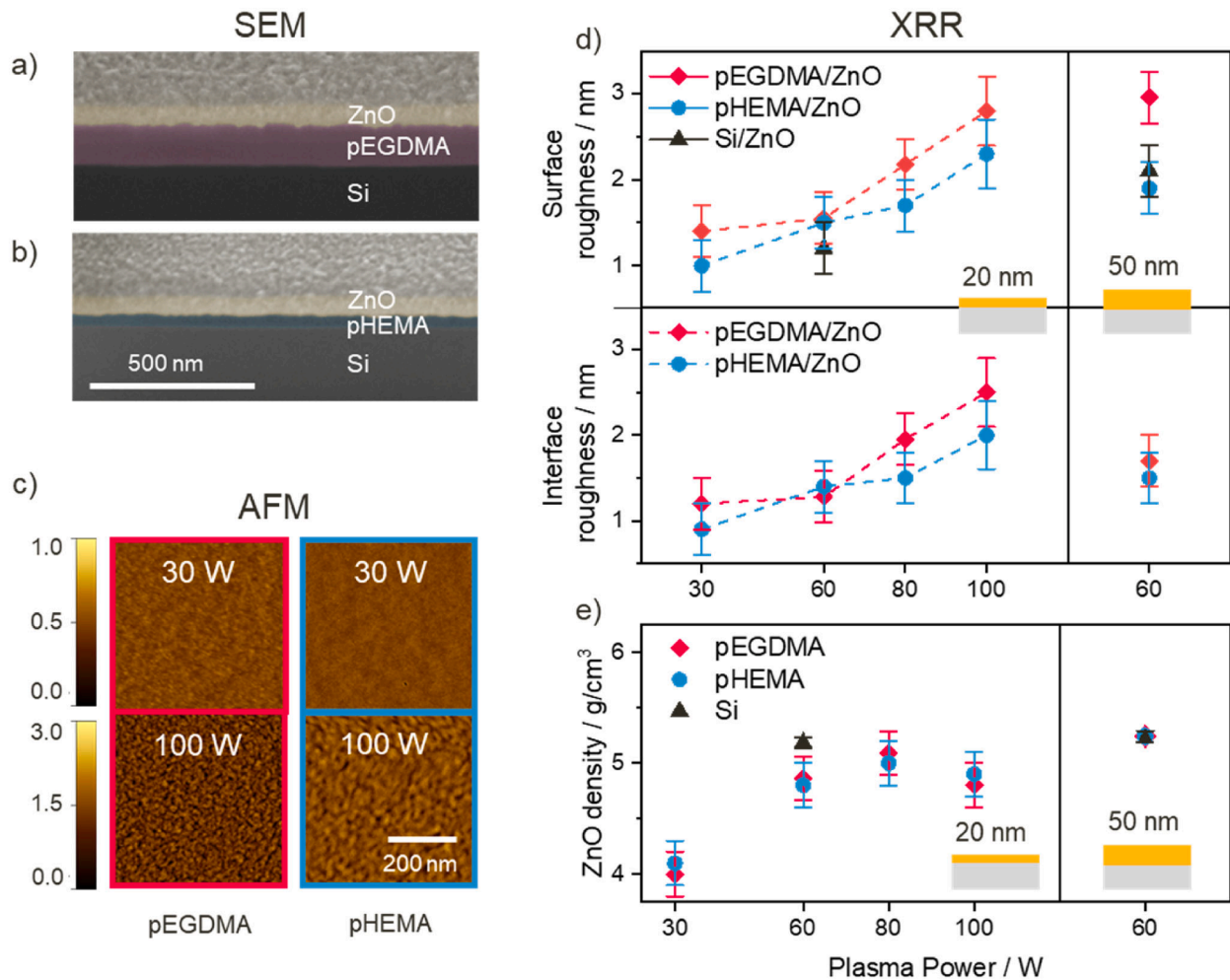


Fig. 6. Interface and surface properties of ZnO films deposited on different substrates at different plasma powers: (a-b) Cross-sectional SEM images of 50-nm ZnO films deposited on (a) pEGDMA and (b) pHEMA at 60 W plasma power. SEM images were recorded at an angle of 52°. (c) AFM images of 20-nm thick ZnO films deposited on pEGDMA and pHEMA at 30 and 100 W plasma power. The height scales are in nanometers. (d) XRR-derived surface and interface roughness and (e) XRR-derived ZnO density values of 20-nm thick (left panel) and 50-nm thick (right panel) ZnO films deposited on pEGDMA, pHEMA and silicon at different plasma powers.

roughness is very low for both substrates and plasma powers between 30 W and 100 W. However, a high plasma power results in a significant increase in surface roughness that is more pronounced for ZnO deposited on pEGDMA than on pHEMA (Fig. 6c).

RMS roughness values calculated from the AFM measurements can be found in Fig. A6 in the supplementary info. This trend is confirmed by the surface roughness values determined from XRR measurements of the same samples (see Fig. 6d) that show an increase in roughness from 1.4 ± 0.3 nm to 2.8 ± 0.4 nm when going from 30 W to 100 W for pEGDMA and an increase from 1.0 ± 0.3 nm to 2.3 ± 0.4 nm for pHEMA. XRR-derived surface roughness values of ZnO thin films grown directly on a silicon substrate at 60 W are in the same range as those of ZnO films grown on pEGDMA and pHEMA under the same conditions (1.2 ± 0.3 nm for silicon and 1.5 ± 0.3 nm for both polymers), indicating that the initial polymer etching does not interfere with the growth of highly uniform ZnO films with very smooth surfaces. XRR measurements can also be used to determine values for the roughness of the interface between the polymer and ZnO layer. The results show that the interface roughness is similar in magnitude to the surface roughness and exhibits the same trend with respect to plasma power. Raising the plasma power from 30 to 100 W increases the interface roughness from 1.2 ± 0.3 nm to 2.5 ± 0.4 nm for pEGDMA and from 0.9 ± 0.3 nm to 2.0 ± 0.4 nm for pHEMA.

The similar trend seen in the interface and surface roughness values suggests that the increased surface roughness at higher plasma powers is primarily a result of the altered interface quality, although differences with plasma power in the nucleation and crystallization behavior of the ZnO itself could also play a role. For example, Pilz et al. [97] demonstrated that the crystallite size decreases from 27 to 20 nm with increasing plasma power. However, these differences might not play a role when film thicknesses are equal or smaller than the expected crystallite size.

For pEGDMA, XRR measurements performed on thicker ZnO films (50 nm) at 60 W plasma power show higher surface roughness values than those performed on the 20-nm thick films at the same plasma power (3.0 ± 0.3 nm instead of 1.5 ± 0.3 nm), while the interface roughness remains unchanged. In the case of ZnO on pHEMA, differences in roughness for the 20 and 50 nm thick films were not significant (1.9 ± 0.3 nm and 1.5 ± 0.3 nm respectively). This increase in surface roughness for thicker films on pEGDMA might be an effect of larger crystallites forming as the layer builds up, an assumption that is confirmed by XRD measurements that will be discussed below.

In terms of ZnO density, XRR measurements show matching densities of approximately 5.24 ± 0.05 g/cm³ (see Fig. 6e) for 50-nm thick ZnO films deposited at 60 W plasma power irrespective of the used substrate (pEGDMA, pHEMA or silicon). This density value is lower than the 5.6 g/cm³ that have been measured previously for PE-ALD ZnO thin films on silicon [75,98], but this variation can be attributed to the use of a different reactor geometry and set of process conditions. For 20-nm thick films, the density of ZnO deposited on one of the polymers is significantly lower with approximately 4.9 ± 0.2 g/cm³ for plasma powers between 60 and 100 W. At 30 W, the measured density is as low as 4.0 ± 0.2 g/cm³. For comparison, a 20-nm thick ZnO film deposited directly on silicon at 60 W results in a density of 5.18 ± 0.05 g/cm³, which is slightly lower than for thicker films but considerably higher than the values measured on polymer. The lower density for thinner ZnO films points to the presence of a density gradient in the layer. This effect is small for growth on silicon, where the substrate is stable and unaffected by the deposition, but larger for growth on one of the polymers. One reason for the lower ZnO density closer to the substrate could be the intermixing of polymer residues with the growing ZnO, stemming either from degradation products of the polymer etching [99,100] or from incomplete removal of the organic precursor ligands [97]. A density gradient for ZnO grown via PE-ALD on silicon was also observed by Perrotta et al. [75].

Finally, the crystallinity of the deposited ZnO films was investigated

via XRD. 50-nm thick ZnO films (Fig. 7a) show identical peak positions on all substrates (pEGDMA, pHEMA and silicon) that agree with previously published results by Pilz et al. [98] who deposited ZnO via PE-ALD on silicon. The (100) ZnO peak is of comparable height on all substrates, while the (002) peak decreases in height when moving from silicon to pHEMA to pEGDMA. The matching peak positions confirm that the ZnO crystal structure is not influenced by the choice of substrate. However, the variation in the (002) peak height suggests that the substrate has some influence on the preferential orientation of the crystallites. Average crystallite sizes were calculated from the (100) peaks by application of Scherrer's formula. The ZnO film deposited on pEGDMA exhibits the largest crystallites with an average size of 23.0 ± 0.4 nm, while crystallite sizes on pHEMA and silicon are slightly lower (21.4 ± 0.2 nm and 21.1 ± 0.4 nm). Pilz et al. [97] measured crystallite sizes of roughly 24 nm for ZnO films deposited on silicon at comparable conditions. As mentioned above, the bigger crystallites in the ZnO films grown on pEGDMA could explain the higher surface roughness compared to films grown on pHEMA and silicon.

The effect of plasma power on the crystallinity is displayed in Fig. 7b for 20-nm ZnO films deposited on pEGDMA. Measurements of ZnO on pHEMA show an almost identical behavior and can be found in Fig. A7 in the supplementary material. The results show that peak heights are similar for plasma powers between 60 and 100 W. This indicates that the

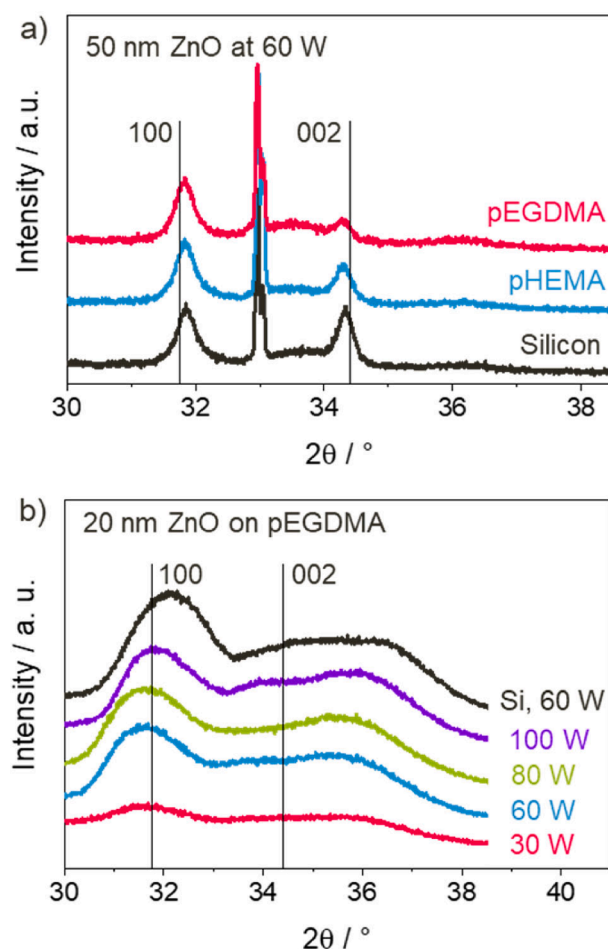


Fig. 7. XRD measurements of ZnO films. (a) $\theta/2\theta$ -scans of 50-nm thick ZnO films deposited on pEGDMA, pHEMA and silicon at 60 W plasma power. The narrow peak at 33° comes from the silicon substrate. (b) $\omega/2\theta$ -scans of 20-nm thick ZnO films deposited on pEGDMA at different plasma powers. Results for ZnO deposited on silicon at 60 W plasma power are shown for reference. Vertical lines indicate the peak positions of a ZnO powder reference (ICSD-26170) [101].

degree of crystallinity in this range is not influenced by the plasma power or the strength of polymer etching. Furthermore, the peak heights agree well with those of ZnO deposited directly on silicon, confirming once more that a similar degree of crystallinity is achieved on all substrates. Compared to ZnO on silicon, peak positions on pEGDMA are slightly shifted to lower angles, which might indicate some degree of strain in the ZnO layer. Similar to the observations made for the ZnO density, the case of 30 W plasma power falls out of line. XRD results show only a very low degree of crystallinity. This low crystallinity together with the lower density reported above fits well with the decreased GPC observed in the ellipsometry data (Fig. 2). As already discussed, the undersaturated GPC is an indication for incomplete surface reactions, i.e. a plasma power of 30 W is not sufficient to completely remove the organic ligands from the adsorbed DEZ molecules. As a result of such incomplete surface reactions, more organic residues will be incorporated into the ZnO film, lowering its density and decreasing its crystallinity.

4. Conclusion

This study investigated PE-ALD growth of ZnO on two different vapor-deposited polymer thin films, poly ethylene glycol dimethacrylate (pEGDMA) and poly 2-hydroxyethyl methacrylate (pHEMA). pHEMA is a hydroxyl-terminated polymer that should provide ample active sites for DEZ precursor adsorption, while pEGDMA is a crosslinked polymer containing only weakly reactive carbonyl-groups. A combination of in-situ ellipsometry and XRR revealed that the initial growth is a consequence of two competing processes: plasma etching of the polymer and ALD growth of ZnO. Three regimes were identified: During regime I, polymer etching dominates, until at a certain point, incipient ZnO nucleation starts to inhibit the etching. This results in a transition regime (II) during which the total thickness (polymer + ZnO) undergoes a minimum. Once etching has subsided completely, regime (III) of ideal, linear ALD growth behavior is entered. The amount and strength of etching was found to be proportional to the applied plasma power as well as dependent on the type of polymer. Observed etching was 35–50 % higher for pHEMA than for pEGDMA. Despite the stronger etching, film formation could already be detected with in-situ ellipsometry and XRR after 3–5 cycles, while on pEGDMA, a delay of 12–16 cycles was observed. In the case of pEGDMA, XRF and XPS results suggested a certain extent of sub-surface diffusion of the DEZ precursor, while film formation on pHEMA appeared to be more surface-limited. This is consistent with previously published results [55,63] that observed enhanced precursor diffusion in polymers with fewer reactive groups. A comparison with the growth models by Puurunen et al. [72] suggested island growth as the dominant growth mode on pEGDMA, while nucleation on pHEMA resembled more that of layer-by-layer growth. These results show that although plasma exposure enhances nucleation through the generation of reactive surface groups, the inherent polymer chemistry still has an influence on the nucleation behavior.

Despite the initial etching, the quality of the resulting thin films at plasma powers between 60 and 100 W was comparable to that of ZnO deposited on silicon in terms of surface roughness (below 3 nm), crystallinity and ZnO density ($5.24 \pm 0.05 \text{ g/cm}^3$ for 50-nm thick films and 60 W). At 30 W plasma power, a lower ZnO density and degree of crystallinity was found, which was attributed to incomplete surface reactions due to an insufficient plasma power. Cross-sectional SEM images of ZnO films deposited on pEGDMA and pHEMA at 60 W plasma power showed a clearly discernible interface between the polymer and the ZnO layer. From this, it can be concluded that the initial etching of the polymer does not significantly affect the formation of high quality ZnO thin films.

The findings of the present study contribute to a deeper understanding of thin film formation during PE-ALD on polymers, which is an important prerequisite for the successful implementation of PE-ALD processes in the design and fabrication of high-quality polymer-based

devices.

CRediT authorship contribution statement

Lisanne Demelius: Conceptualization, Methodology, Investigation, Formal analysis, Validation, Visualization, Writing – original draft. **Matthias Blatnik:** Investigation, Formal analysis, Validation, Writing – review & editing. **Katrin Unger:** Methodology, Writing – review & editing, Supervision. **Paola Parlanti:** Investigation, Formal analysis. **Mauro Gemmi:** Investigation, Formal analysis. **Anna Maria Coclite:** Conceptualization, Writing – review & editing, Supervision, Funding acquisition.

Declaration of Competing Interest

The authors declare that they have no known competing financial interests or personal relationships that could have appeared to influence the work reported in this paper.

Acknowledgments

This project has received funding from the European Union's Horizon 2020 research and innovation programme under grant agreement No. 899349.

M. B. gratefully acknowledges CzechNanoLab project LM2018110 funded by MEYS CR for the financial support of the measurements at CEITEC Nano Research Infrastructure.

Appendix A. Supplementary material

The following are the Supplementary data to this article and include: In-situ ellipsometry results for growth on silicon, XRR original data with fits, XPS C1s peaks, AFM RMS roughness, XRD results for pHEMA. Supplementary data to this article can be found online at <https://doi.org/10.1016/j.apsusc.2022.154619>.

References

- [1] R.W. Johnson, A. Hultqvist, S.F. Bent, A brief review of atomic layer deposition: from fundamentals to applications, *Mater. Today*. 17 (2014) 236–246, <https://doi.org/10.1016/j.mattod.2014.04.026>.
- [2] P.D. Ye, G.D. Wilk, J. Kwo, B. Yang, H.-J.-L. Gossman, M. Frei, S.N.G. Chu, J. P. Mannaerts, M. Sergeant, M. Hong, K.K. Ng, J. Bude, GaAs MOSFET with oxide gate dielectric grown by atomic layer deposition, *IEEE Electron Device Lett.* 24 (2003) 209–211, <https://doi.org/10.1109/LED.2003.812144>.
- [3] M. Bohr, R. Chau, T. Ghani, K. Mistry, The High-k Solution, *IEEE Spectr.* 44 (2007) 29–35, <https://doi.org/10.1109/MSPEC.2007.4337663>.
- [4] J.A. Raiford, S.T. Oyakhire, S.F. Bent, Applications of atomic layer deposition and chemical vapor deposition for perovskite solar cells, *Energy Environ. Sci.* 13 (2020) 1997–2023, <https://doi.org/10.1039/D0EE000385A>.
- [5] W. Niu, X. Li, S.K. Karuturi, D.W. Fam, H. Fan, S. Shrestha, L.H. Wong, A.I.Y. Tok, Applications of atomic layer deposition in solar cells, *Nanotechnology*. 26 (2015), 064001, <https://doi.org/10.1088/0957-4484/26/6/064001>.
- [6] J.A. van Delft, D. Garcia-Alonso, W.M.M. Kessels, Atomic layer deposition for photovoltaics: applications and prospects for solar cell manufacturing, *Semicond. Sci. Technol.* 27 (2012) 074002, <https://doi.org/10.1088/0268-1242/27/7/074002>.
- [7] L.J. Sutherland, H.C. Weerasinghe, G.P. Simon, A Review on Emerging Barrier Materials and Encapsulation Strategies for Flexible Perovskite and Organic Photovoltaics, *Adv. Energy Mater.* 11 (2021) 1–32, <https://doi.org/10.1002/aenm.202101383>.
- [8] S.K. Kim, G.-J. Choi, S.Y. Lee, M. Seo, S.W. Lee, J.H. Han, H.-S. Ahn, S. Han, C. S. Hwang, Al-Doped TiO₂ Films with Ultralow Leakage Currents for Next Generation DRAM Capacitors, *Adv. Mater.* 20 (2008) 1429–1435, <https://doi.org/10.1002/adma.200701085>.
- [9] P.O. Oviroh, R. Akbarzadeh, D. Pan, R.A.M. Coetzee, T.-C. Jen, New development of atomic layer deposition: processes, methods and applications, *Sci. Technol. Adv. Mater.* 20 (2019) 465–496, <https://doi.org/10.1080/14686996.2019.1599694>.
- [10] A.J. Pearce, T.E. Schmitt, E.J. Fuller, F. El-Gabaly, C.-F. Lin, K. Gerasopoulos, A. C. Kozen, A.A. Talin, G. Rubloff, K.E. Gregorczyk, Nanoscale Solid State Batteries Enabled by Thermal Atomic Layer Deposition of a Lithium Polyphosphazene Solid State Electrolyte, *Chem. Mater.* 29 (2017) 3740–3753, <https://doi.org/10.1021/acs.chemmater.7b00805>.

- [11] M. Létiche, E. Eustache, J. Freixas, A. Demortière, V. De Andrade, L. Morgenroth, P. Tilmant, F. Vaurette, D. Troade, P. Roussel, T. Brousse, C. Lethien, Atomic Layer Deposition of Functional Layers for on Chip 3D Li-Ion All Solid State Microbattery, *Adv. Energy Mater.* 7 (2017) 1601402, <https://doi.org/10.1002/aenm.201601402>.
- [12] D. Go, J.W. Shin, S. Lee, J. Lee, B.C. Yang, Y. Won, M. Motoyama, J. An, Atomic Layer Deposition for Thin Film Solid-State Battery and Capacitor, *Int. J. Precis. Eng. Manuf. Technol.* (2022), <https://doi.org/10.1007/s40684-022-00419-x>.
- [13] Atomic Limits ALD Database, (n.d.). <https://doi.org/10.6100/alddbatabase>.
- [14] T. Tynell, M. Karppinen, Atomic layer deposition of ZnO: a review, *Semicond. Sci. Technol.* 29 (2014), 043001, <https://doi.org/10.1088/0268-1242/29/4/043001>.
- [15] K.L. Jarvis, P.J. Evans, Growth of thin barrier films on flexible polymer substrates by atomic layer deposition, *Thin Solid Films* 624 (2017) 111–135, <https://doi.org/10.1016/j.tsf.2016.12.055>.
- [16] T. Hirvikorpi, M. Vähä-Nissi, A. Harlin, M. Karppinen, Comparison of some coating techniques to fabricate barrier layers on packaging materials, *Thin Solid Films* 518 (2010) 5463–5466, <https://doi.org/10.1016/j.tsf.2010.04.018>.
- [17] M. Shahmohammadi, B.E. Nagay, V.A.R. Barão, C. Sukotjo, G. Jursich, C. G. Takoudis, Atomic layer deposition of TiO₂, ZnO and TiO₂/ZnO mixed oxide nanofilms on PMMA for enhanced biomaterial functionalization, *Appl. Surf. Sci.* 578 (2022), <https://doi.org/10.1016/j.apsusc.2021.151891>.
- [18] N.A. Vogel, P.S. Williams, A.H. Brozena, D. Sen, S. Atanasov, G.N. Parsons, S. A. Khan, Delayed Dissolution and Small Molecule Release from Atomic Layer Deposition Coated Electrospun Nanofibers, *Adv. Mater. Interfaces* 2 (2015) 1500229, <https://doi.org/10.1002/admi.201500229>.
- [19] P. Paul, K. Pfeiffer, A. Szezhalmi, Antireflection Coating on PMMA Substrates by Atomic Layer Deposition, *Coatings* 10 (2020) 64, <https://doi.org/10.3390/coatings10010064>.
- [20] Y. Kawamura, M. Tani, N. Hattori, N. Miyatake, M. Horita, Y. Ishikawa, Y. Uraoka, Low-Temperature-Processed Zinc Oxide Thin-Film Transistors Fabricated by Plasma-Assisted Atomic Layer Deposition, *Jpn. J. Appl. Phys.* 51 (2012) 02BF04, <https://doi.org/10.1143/JJAP.51.02BF04>.
- [21] J.M. Kim, T. Nam, S.J. Lim, Y.G. Seol, N.E. Lee, D. Kim, H. Kim, Atomic layer deposition ZnO: N flexible thin film transistors and the effects of bending on device properties, *Appl. Phys. Lett.* 98 (2011) 1–4, <https://doi.org/10.1063/1.3577607>.
- [22] Y.Y. Lin, C.C. Hsu, M.H. Tseng, J.J. Shyue, F.Y. Tsai, Stable and High-Performance Flexible ZnO Thin-Film Transistors by Atomic Layer Deposition, *ACS Appl. Mater. Interfaces* 7 (2015) 22610–22617, <https://doi.org/10.1021/acsami.5b07278>.
- [23] J.C. Wang, W.T. Weng, M.Y. Tsai, M.K. Lee, S.F. Horng, T.P. Perng, C.C. Kei, C. C. Yu, H.F. Meng, Highly efficient flexible inverted organic solar cells using atomic layer deposited ZnO as electron selective layer, *J. Mater. Chem.* 20 (2010) 862–866, <https://doi.org/10.1039/b921396a>.
- [24] H. Cheun, C. Fuentes-Hernandez, Y. Zhou, W.J. Potscavage, S.J. Kim, J. Shim, A. Dindar, B. Kippelen, Electrical and optical properties of ZnO processed by atomic layer deposition in inverted polymer solar cells, *J. Phys. Chem. C* 114 (2010) 20713–20718, <https://doi.org/10.1021/jp106641j>.
- [25] A. Shimizu, S. Chaisitsak, T. Sugiyama, A. Yamada, M. Konagai, Zinc-based buffer layer in the Cu(InGa)Se₂ thin film solar cells, *Thin Solid Films* 361 (2000) 193–197, [https://doi.org/10.1016/S0040-6090\(99\)00792-0](https://doi.org/10.1016/S0040-6090(99)00792-0).
- [26] S. Chaisitsak, T. Sugiyama, A. Yamada, M. Konagai, Cu(InGa)Se₂ Thin-film Solar Cells with High Resistivity ZnO Buffer Layers Deposited by Atomic Layer Deposition, *Jpn. J. Appl. Phys.* Part 1 Regul. Pap. Short Notes Rev. Pap. 38 (1999) 4989–4992, <https://doi.org/10.1143/jjap.38.4989>.
- [27] M. Law, L.E. Greene, J.C. Johnson, R. Saykally, P. Yang, Nanowire dye-sensitized solar cells, *Nat. Mater.* 4 (2005) 455–459, <https://doi.org/10.1038/nmat1387>.
- [28] A.B.F. Martinson, J.W. Elam, J.T. Hupp, M.J. Pellin, ZnO nanotube based dye-sensitized solar cells, *Nano Lett.* 7 (2007) 2183–2187, <https://doi.org/10.1021/nl070160+>.
- [29] X. Jiang, F.L. Wong, M.K. Fung, S.T. Lee, Aluminum-doped zinc oxide films as transparent conductive electrode for organic light-emitting devices, *Appl. Phys. Lett.* 83 (2003) 1875–1877, <https://doi.org/10.1063/1.1605805>.
- [30] H. Kim, C.M. Gilmore, J.S. Horwitz, A. Piqué, H. Murata, G.P. Kushto, R. Schlaf, Z. H. Kafafi, D.B. Chrisey, Transparent conducting aluminum-doped zinc oxide thin films for organic light-emitting devices, *Appl. Phys. Lett.* 76 (2000) 259–261, <https://doi.org/10.1063/1.125740>.
- [31] H. Saarenpää, T. Niemi, A. Tukiainen, H. Lemmetyinen, N. Tkachenko, Aluminum doped zinc oxide films grown by atomic layer deposition for organic photovoltaic devices, *Sol. Energy Mater. Sol. Cells* 94 (2010) 1379–1383, <https://doi.org/10.1016/j.solmat.2010.04.006>.
- [32] C. Wang, L. Yin, L. Zhang, D. Xiang, R. Gao, Metal oxide gas sensors: Sensitivity and influencing factors, *Sensors* 10 (2010) 2088–2106, <https://doi.org/10.3390/s100302088>.
- [33] U. Singh, H.A. Lee, Y.C. Byun, A. Kumar, S. Seal, H. Kim, H.J. Cho, ZnO modified high aspect ratio carbon electrodes for hydrogen sensing applications, *Procedia Eng.* 25 (2011) 1669–1672, <https://doi.org/10.1016/j.proeng.2011.12.413>.
- [34] C. Sun, J. Zhang, Y. Zhang, F. Zhao, J. Xie, Z. Liu, J. Zhuang, N. Zhang, W. Ren, Z.-G. Ye, Design and fabrication of flexible strain sensor based on ZnO-decorated PVDF via atomic layer deposition, *Appl. Surf. Sci.* 562 (2021) 150126, <https://doi.org/10.1016/j.apsusc.2021.150126>.
- [35] C.A. Wilson, R.K. Grubbs, S.M. George, Nucleation and Growth during Al₂O₃ Atomic Layer Deposition on Polymers, *Chem. Mater.* 17 (2005) 5625–5634, <https://doi.org/10.1021/cm050704d>.
- [36] G.N. Parsons, S.E. Atanasov, E.C. Dandley, C.K. Devine, B. Gong, J.S. Jur, K. Lee, C.J. Oldham, Q. Peng, J.C. Spagnola, P.S. Williams, Mechanisms and reactions during atomic layer deposition on polymers, *Coord. Chem. Rev.* 257 (2013) 3323–3331, <https://doi.org/10.1016/j.ccr.2013.07.001>.
- [37] C.Z. Leng, M.D. Losego, Vapor phase infiltration (VPI) for transforming polymers into organic-inorganic hybrid materials: A critical review of current progress and future challenges, *Mater. Horizons* 4 (2017) 747–771, <https://doi.org/10.1039/c7mh00196g>.
- [38] D.H. Yi, C.-Y. Nam, G. Doerk, C.T. Black, R.B. Grubbs, Infiltration Synthesis of Diverse Metal Oxide Nanostructures from Epoxidized Diene-Styrene Block Copolymer Templates, *ACS Appl. Polym. Mater.* 1 (2019) 672–683, <https://doi.org/10.1021/acsapm.8b00138>.
- [39] Y. Chen, N.J. Ginga, W.S. LePage, E. Kazyak, A.J. Gayle, J. Wang, R.E. Rodríguez, M.D. Thouless, N.P. Dasgupta, Enhanced Interfacial Toughness of Thermoplastic-Epoxy Interfaces Using ALD Surface Treatments, *ACS Appl. Mater. Interfaces* 11 (2019) 43573–43580, <https://doi.org/10.1021/acsami.9b15193>.
- [40] J. Pilz, A.M. Coclite, M.D. Losego, Vapor phase infiltration of zinc oxide into thin films of cis-polyisoprene rubber, *Mater. Adv.* 1 (2020) 1695–1704, <https://doi.org/10.1039/d0ma00304b>.
- [41] Y. Ren, E.K. McGuinness, C. Huang, V.R. Joseph, R.P. Lively, M.D. Losego, Reaction-diffusion transport model to predict precursor uptake and spatial distribution in vapor-phase infiltration processes, *Chem. Mater.* 33 (2021) 5210–5222, <https://doi.org/10.1021/acs.chemmater.1c01283>.
- [42] B. Gong, G.N. Parsons, Quantitative in situ infrared analysis of reactions between trimethylaluminum and polymers during Al₂O₃ atomic layer deposition, *J. Mater. Chem.* 22 (2012) 15672–15682, <https://doi.org/10.1039/c2jm32343e>.
- [43] A. Mamel, B. Karasulu, M.A. Verheijen, B. Barcones, B. Maccio, A.J.M. Mackus, W.M.M.E. Kessels, F. Roozeboom, Area-Selective Atomic Layer Deposition of ZnO by Area Activation Using Electron Beam-Induced Deposition, *Chem. Mater.* 31 (2019) 1250–1257, <https://doi.org/10.1021/acs.chemmater.8b03165>.
- [44] Q. Peng, Y.C. Tseng, S.B. Darling, J.W. Elam, A route to nanoscopic materials via sequential infiltration synthesis on block copolymer templates, *ACS Nano* 5 (2011) 4600–4606, <https://doi.org/10.1021/nn2003234>.
- [45] B. Gong, Q. Peng, J.S. Jur, C.K. Devine, K. Lee, G.N. Parsons, Sequential vapor infiltration of metal oxides into sacrificial polyester fibers: Shape replication and controlled porosity of microporous/mesoporous oxide monoliths, *Chem. Mater.* 23 (2011) 3476–3485, <https://doi.org/10.1021/cm200694w>.
- [46] X. Ye, J. Kestell, K. Kisslinger, M. Liu, R.B. Grubbs, J.A. Boscoboinik, C.Y. Nam, Effects of Residual Solvent Molecules Facilitating the Infiltration Synthesis of ZnO in a Nonreactive Polymer, *Chem. Mater.* 29 (2017) 4535–4545, <https://doi.org/10.1021/acs.chemmater.7b01222>.
- [47] S. Obuchovsky, I. Deckman, M. Moshonov, T. Segal Peretz, G. Ankonina, T. J. Savenije, G.L. Frey, Atomic layer deposition of zinc oxide onto and into P3HT for hybrid photovoltaics, *J. Mater. Chem. C* 2 (2014) 8903–8910, <https://doi.org/10.1039/c4tc01629g>.
- [48] C.S. Lee, J. Kim, J.Y. Son, W. Choi, H. Kim, Photocatalytic functional coatings of TiO₂ thin films on polymer substrate by plasma enhanced atomic layer deposition, *Appl. Catal. B Environ.* 91 (2009) 628–633, <https://doi.org/10.1016/j.apcatb.2009.06.037>.
- [49] L.C. Wang, Y.Y. Han, K.C. Yang, M.J. Chen, H.C. Lin, C.K. Lin, Y.T. Hsu, Hydrophilic/hydrophobic surface of Al₂O₃ thin films grown by thermal and plasma-enhanced atomic layer deposition on plasticized polyvinyl chloride (PVC), *Surf. Coatings Technol.* 305 (2016) 158–164, <https://doi.org/10.1016/j.surfcoat.2016.08.023>.
- [50] G.A. Ten Eyck, S. Pimanpang, J.S. Juneja, H. Bakhru, T.M. Lu, G.C. Wang, Plasma-enhanced atomic layer deposition of palladium on a polymer substrate, *Chem. Vap. Depos.* 13 (2007) 307–311, <https://doi.org/10.1002/cvde.200606508>.
- [51] M. Gebhard, F. Mitscher, C. Hoppe, M. Aghaee, D. Rogalla, M. Creatore, G. Grundmeier, P. Awakowicz, A. Devi, A combinatorial approach to enhance barrier properties of thin films on polymers: Seeding and capping of PECVD thin films by PEALD, *Plasma Process. Polym.* 15 (2018) 1–11, <https://doi.org/10.1002/ppap.201700209>.
- [52] S.J. Yun, Y.W. Ko, J.W. Lim, Passivation of organic light-emitting diodes with aluminum oxide thin films grown by plasma-enhanced atomic layer deposition, *Appl. Phys. Lett.* 85 (2004) 4896–4898, <https://doi.org/10.1063/1.1826238>.
- [53] E. Langereis, M. Creatore, S.B.S. Heil, M.C.M. Van De Sanden, W.M.M. Kessels, Plasma-assisted atomic layer deposition of Al₂O₃ moisture permeation barriers on polymers, *Appl. Phys. Lett.* 89 (2006) 1–4, <https://doi.org/10.1063/1.2338776>.
- [54] L.H. Kim, J.H. Jang, Y.J. Jeong, K. Kim, Y. Baek, H. jin Kwon, T.K. An, S. Nam, S. H. Kim, J. Jang, C.E. Park, Highly-impermeable Al₂O₃/HfO₂ moisture barrier films grown by low-temperature plasma-enhanced atomic layer deposition, *Org. Electron.* 50 (2017) 296–303, <https://doi.org/10.1016/j.orgel.2017.07.051>.
- [55] A. Perrotta, C. Fuentes-Hernandez, T.M. Khan, B. Kippelen, M. Creatore, S. Graham, Near room-temperature direct encapsulation of organic photovoltaics by plasma-based deposition techniques, *J. Phys. D: Appl. Phys.* 50 (2017) 024003, <https://doi.org/10.1088/1361-6463/50/2/024003>.
- [56] K.L. Jarvis, P.J. Evans, A. Nelson, G. Triani, Comparisons of alumina barrier films deposited by thermal and plasma atomic layer deposition, *Mater. Today Chem.* 11 (2019) 8–15, <https://doi.org/10.1016/j.mtchem.2018.10.002>.
- [57] N. Inagaki, S. Tasaka, K. Narushima, H. Kobayashi, Surface modification of PET films by pulsed argon plasma, *J. Appl. Polym. Sci.* 85 (2002) 2845–2852, <https://doi.org/10.1002/app.10865>.
- [58] K.N. Pandiyaraj, V. Selvarajan, R.R. Deshmukh, M. Bousmina, The effect of glow discharge plasma on the surface properties of Poly (ethylene terephthalate) (PET) film, *Surf. Coatings Technol.* 202 (2008) 4218–4226, <https://doi.org/10.1016/j.surfcoat.2008.03.015>.

- [59] B. Ozkaya, S. Grosse-Kreul, C. Corbella, A. Von Keudell, G. Grundmeier, Combined in situ XPS and UHV-chemical force microscopy (CFM) studies of the plasma induced surface oxidation of polypropylene, *Plasma Process. Polym.* 11 (2014) 256–262, <https://doi.org/10.1002/ppap.201300105>.
- [60] N.Y. Cui, N.M.D. Brown, Modification of the surface properties of a polypropylene (PP) film using an air dielectric barrier discharge plasma, *Appl. Surf. Sci.* 189 (2002) 31–38, [https://doi.org/10.1016/S0169-4332\(01\)01035-2](https://doi.org/10.1016/S0169-4332(01)01035-2).
- [61] M. Napari, M. Lahtinen, A. Veselov, J. Julin, E. Östreng, T. Sajavaara, Room-temperature plasma-enhanced atomic layer deposition of ZnO: Film growth dependence on the PEALD reactor configuration, *Surf. Coatings Technol.* 326 (2017) 281–290, <https://doi.org/10.1016/j.surfcoat.2017.07.056>.
- [62] M. Napari, J. Malm, R. Lehto, J. Julin, K. Arstila, T. Sajavaara, M. Lahtinen, Nucleation and growth of ZnO on PMMA by low-temperature atomic layer deposition, *J. Vac. Sci. Technol. A Vacuum, Surfaces, Film.* 33 (2015) 01A128, <https://doi.org/10.1116/1.4902326>.
- [63] A. Bulusu, S. Graham, H. Bahre, H. Behm, M. Böke, R. Dahlmann, C. Hopmann, J. Winter, The Mechanical Behavior of ALD-Polymer Hybrid Films Under Tensile Strain, *Adv. Eng. Mater.* 17 (2015) 1057–1067, <https://doi.org/10.1002/adem.201400431>.
- [64] A.S. Da Silva Sobrinho, J. Chasle, G. Drenner, M.R. Wertheimer, Characterization of defects in PECVD-SiO₂ coatings on PET by confocal microscopy, *Plasma Polym.* 3 (1998) 231–247, <https://doi.org/10.1023/A:1021854805605>.
- [65] M. Gebhard, L. Mai, L. Banko, F. Mitschker, C. Hoppe, M. Jaritz, D. Kirchheim, C. Zekorn, T. De Los Arcos, D. Grochla, R. Dahlmann, G. Grundmeier, P. Awakowicz, A. Ludwig, H. Bahre, H. Behm, M. Böke, R. Dahlmann, C. Hopmann, J. Winter, The Mechanical Behavior of ALD-Polymer Hybrid Films Under Tensile Strain, *Adv. Eng. Mater.* 17 (2015) 1057–1067, <https://doi.org/10.1002/adem.201400431>.
- [66] C. Ranacher, R. Resel, P. Moni, B. Cermenek, V. Hacker, A.M. Coclite, Layered Nanostructures in Proton Conductive Polymers Obtained by Initiated Chemical Vapor Deposition, *Macromolecules* 48 (2015) 6177–6185, <https://doi.org/10.1021/acs.macromol.5b01145>.
- [67] T. Abu Ali, P. Schäffner, M. Belegatis, G. Schider, B. Stadlober, A.M. Coclite, Smart Core-Shell Nanostructures for Force, Humidity, and Temperature Multi-Stimuli Responsiveness, *Adv. Mater. Technol.* 2200246 (2022) 2200246, <https://doi.org/10.1002/admt.202200246>.
- [68] M. Birkholz, Thin film analysis by X-ray scattering, Wiley-VCH, Weinheim, 2006 <https://permalink.obvsg.at/tug/AC04655566>.
- [69] D. Nečas, P. Klapetek, Gwyddion: an open-source software for SPM data analysis, *Open Phys.* 10 (2012) 181–188, <https://doi.org/10.2478/s11534-011-0096-2>.
- [70] E. Langereis, S.B.S. Heil, H.C.M. Knoops, W. Keuning, M.C.M. van de Sanden, W. M.M. Kessels, In situ spectroscopic ellipsometry as a versatile tool for studying atomic layer deposition, *J. Phys. D: Appl. Phys.* 42 (2009) 073001, <https://doi.org/10.1088/0022-3727/42/7/073001>.
- [71] E.V. Skopin, J.L. Deschamps, H. Renevier, In Situ Ellipsometry Study of the Early Stage of ZnO Atomic Layer Deposition on In_{0.53}Ga_{0.47}As, *Phys. Status Solidi Appl. Mater. Sci.* 217 (2020) 1–6, <https://doi.org/10.1002/pssa.201900831>.
- [72] R.L. Puurunen, W. Vandervorst, Island growth as a growth mode in atomic layer deposition: A phenomenological model, *J. Appl. Phys.* 96 (2004) 7686–7695, <https://doi.org/10.1063/1.1810193>.
- [73] G.P. Gakis, C. Vahlas, E. Vergnes, S. Dourdain, Y. Tison, H. Martinez, J. Bour, D. Ruch, A.G. Boudouvis, B. Caussat, E. Scheid, Investigation of the initial deposition steps and the interfacial layer of Atomic Layer Deposited (ALD) Al₂O₃ on Si, *Appl. Surf. Sci.* 492 (2019) 245–254, <https://doi.org/10.1016/j.apsusc.2019.06.215>.
- [74] G.P. Gakis, H. Vergnes, F. Cristiano, Y. Tison, C. Vahlas, B. Caussat, A. G. Boudouvis, E. Scheid, In situ N₂-NH₃ plasma pre-treatment of silicon substrate enhances the initial growth and restricts the substrate oxidation during alumina ALD, *J. Appl. Phys.* 126 (2019), <https://doi.org/10.1063/1.5113755>.
- [75] A. Perrotta, J. Pilz, R. Resel, O. Werzer, A.M. Coclite, Initial Growth and Crystallization Onset of Plasma Enhanced-Atomic Layer Deposited ZnO, *Crystals* 10 (2020) 291, <https://doi.org/10.3390/cryst10040291>.
- [76] Z. Baji, Z. Lábadi, Z.E. Horváth, G. Molnár, J. Volk, I. Bársony, P. Barna, Nucleation and growth modes of ALD ZnO, *Cryst. Growth Des.* 12 (2012) 5615–5620, <https://doi.org/10.1021/cg301129v>.
- [77] R.-H. Chang, K.-C. Yang, T.-H. Chen, L.-W. Lai, T.-H. Lee, S.-L. Yao, D.-S. Liu, Surface Modification on the Sputtering-Deposited ZnO Layer for ZnO-Based Schottky Diode, *J. Nanomater.* 2013 (2013) 1–9, <https://doi.org/10.1155/2013/560542>.
- [78] I. Fidelis, C. Stiehler, M. Duarte, C. Enderlein, W.S. Silva, E.A. Soares, S. Shaikhutdinov, H.J. Freund, F. Stavale, Electronic properties of ultrathin O-terminated ZnO (0001)̄, *Surf. Sci.* 679 (2019) 259–263, <https://doi.org/10.1016/j.susc.2018.10.007>.
- [79] M.P.F. de Godoy, L.K.S. de Herval, A.A.C. Cotta, Y.J. Onofre, W.A.A. Macedo, ZnO thin films design: the role of precursor molarity in the spray pyrolysis process, *J. Mater. Sci. Mater. Electron.* 31 (2020) 17269–17280, <https://doi.org/10.1007/s10854-020-04281-y>.
- [80] J.S. Kim, H.A. Marzouk, P.J. Reucroft, C.E. Hamrin, Characterization of high quality c axis oriented ZnO thin films grown by metal organic chemical vapor deposition using zinc acetate as source material, *Thin Solid Films* 217 (1992) 133–137, [https://doi.org/10.1016/0040-6090\(92\)90619-M](https://doi.org/10.1016/0040-6090(92)90619-M).
- [81] L.S. Dake, D.R. Baer, J.M. Zachara, Auger parameter measurements of zinc compounds relevant to zinc transport in the environment, *Surf. Interface Anal.* 14 (1989) 71–75, <https://doi.org/10.1002/sia.740140115>.
- [82] G. Deroubaix, P. Marcus, X-ray photoelectron spectroscopy analysis of copper and zinc oxides and sulphides, *Surf. Interface Anal.* 18 (1992) 39–46, <https://doi.org/10.1002/sia.740180107>.
- [83] A.G. Marrani, F. Caprioli, A. Boccia, R. Zanon, F. Decker, Electrochemically deposited ZnO films: An XPS study on the evolution of their surface hydroxide and defect composition upon thermal annealing, *J. Solid State Electrochem.* (2014) 505–513, <https://doi.org/10.1007/s10008-013-2281-2>.
- [84] L.E. Ocola, A. Connolly, D.J. Gosztola, R.D. Schaller, A. Yanguas-Gil, Infiltrated Zinc Oxide in Poly(methyl methacrylate): An Atomic Cycle Growth Study, *J. Phys. Chem. C* 121 (2017) 1893–1903, <https://doi.org/10.1021/acs.jpcc.6b08007>.
- [85] S. Tougaard, Practical guide to the use of backgrounds in quantitative XPS, *J. Vac. Sci. Technol. A* 39 (2021) 011201, <https://doi.org/10.1116/6.0000661>.
- [86] S. Tougaard, Composition depth information from the inelastic background signal in XPS, *Surf. Sci.* 162 (1985) 875–885, [https://doi.org/10.1016/0039-6028\(85\)90992-6](https://doi.org/10.1016/0039-6028(85)90992-6).
- [87] S. Tougaard, X-ray photoelectron spectroscopy peak shape analysis for the extraction of in-depth composition information, *J. Vac. Sci. Technol. A Vacuum, Surfaces, Film.* 5 (1987) 1275–1278, <https://doi.org/10.1116/1.574789>.
- [88] D. Briggs, D. Rance, C. Kendall, A. Blythe, Surface modification of poly(ethylene terephthalate) by electrical discharge treatment, *Polymer (Guildf)* 21 (1980) 895–900, [https://doi.org/10.1016/0032-3861\(80\)90244-X](https://doi.org/10.1016/0032-3861(80)90244-X).
- [89] G.P. López, B.D. Ratner, Substrate temperature effects on film chemistry in plasma depositions of organics. II. Polymerizable precursors, *J. Polym. Sci. Part A, Polym. Chem.* 30 (1992) 2415–2425, <https://doi.org/10.1002/pola.1992.080301116>.
- [90] G.P. López, D.G. Castner, B.D. Ratner, XPS O 1s binding energies for polymers containing hydroxyl, ether, ketone and ester groups, *Surf. Interface Anal.* 17 (1991) 267–272, <https://doi.org/10.1002/sia.740170508>.
- [91] K. Aramaki, Self-healing mechanism of a protective film prepared on a Ce(NO₃)₃-pretreated zinc electrode by modification with Zn(NO₃)₂ and Na₃PO₄, *Corros. Sci.* 45 (2003) 1085–1101, [https://doi.org/10.1016/S0010-938X\(02\)00153-1](https://doi.org/10.1016/S0010-938X(02)00153-1).
- [92] Z. Shi, S. Zhang, B. Wu, X. Cai, J. Zhang, W. Yin, H. Wang, J. Wang, X. Xia, X. Dong, B. Zhang, G. Du, Oxygen-induced physical property variation of deposited ZnO films by metal-organic chemical vapor deposition, *Appl. Surf. Sci.* 258 (2012) 8673–8677, <https://doi.org/10.1016/j.apsusc.2012.05.072>.
- [93] C. Li, H. Liang, J. Zhao, Q. Feng, J. Bian, Y. Liu, R. Shen, W. Li, G. Wu, G.T. Du, Influence of high-pressure hydrogen treatment on structural and electrical properties of ZnO thin films, *Appl. Surf. Sci.* 256 (2010) 6770–6774, <https://doi.org/10.1016/j.apsusc.2010.04.087>.
- [94] J.V. Lauritsen, S. Porsgaard, M.K. Rasmussen, M.C.R. Jensen, R. Bechstein, K. Meinander, B.S. Clausen, S. Helveg, R. Wahl, G. Kresse, F. Besenbacher, Stabilization principles for polar surfaces of ZnO, *ACS Nano* 5 (2011) 5987–5994, <https://doi.org/10.1021/nn2017606>.
- [95] Z. Zhao, J.L. Song, J.H. Zheng, J.S. Lian, Optical properties and photocatalytic activity of Nd-doped ZnO powders, *Trans. Nonferrous Met. Soc. China (English Ed.)* 24 (2014) 1434–1439, [https://doi.org/10.1016/S1003-6326\(14\)63209-X](https://doi.org/10.1016/S1003-6326(14)63209-X).
- [96] T.B. Hur, G.S. Jeon, Y.H. Hwang, H.K. Kim, Photoluminescence of polycrystalline ZnO under different annealing conditions, *J. Appl. Phys.* 94 (2003) 5787–5790, <https://doi.org/10.1063/1.1617357>.
- [97] J. Pilz, A. Perrotta, P. Christian, M. Tazreiter, R. Resel, G. Leising, T. Griesser, A. M. Coclite, Tuning of material properties of ZnO thin films grown by plasma-enhanced atomic layer deposition at room temperature, *J. Vac. Sci. Technol. A Vacuum, Surfaces, Film.* 36 (2018) 01A109, <https://doi.org/10.1116/1.5003334>.
- [98] J. Pilz, A. Perrotta, G. Leising, A.M. Coclite, ZnO Thin Films Grown by Plasma-Enhanced Atomic Layer Deposition: Material Properties Within and Outside the “Atomic Layer Deposition Window”, *Phys. Status Solidi Appl. Mater. Sci.* 217 (2020) 1–8, <https://doi.org/10.1002/pssa.201900256>.
- [99] Y. Park, N. Inagaki, Surface modification of poly(vinylidene fluoride) film by remote Ar, H₂, and O₂ plasmas, *Polymer (Guildf)* 44 (2003) 1569–1575, [https://doi.org/10.1016/S0032-3861\(02\)00872-8](https://doi.org/10.1016/S0032-3861(02)00872-8).
- [100] H.C.M. Knoops, K. de Peuter, W.M.M. Kessels, Redeposition in plasma-assisted atomic layer deposition: Silicon nitride film quality ruled by the gas residence time, *Appl. Phys. Lett.* 107 (2015) 014102, <https://doi.org/10.1063/1.4926366>.
- [101] S.C. Abrahams, J.L. Bernstein, Remeasurement of the structure of hexagonal ZnO, *Acta Crystallogr. Sect. B Struct. Crystallogr. Cryst. Chem.* 25 (1969) 1233–1236, <https://doi.org/10.1107/s0567740869003876>.